January 2018

Determining The Correlation Significance Between S-Type Asteroid Orbital Inclination And Albedo Attributable To Space Weathering

Benjamin Wright Mcgee

DETERMINING THE CORRELATION SIGNIFICANCE BETWEEN S-TYPE ASTEROID ORBITAL INCLINATION AND ALBEDO ATTRIBUTABLE TO SPACE WEATHERING

by

Benjamin Wright McGee
Bachelor of Science, University of Wyoming, 2005

A Thesis
Submitted to the Graduate Faculty

of the

University of North Dakota

In partial fulfillment of the requirements

for the degree of

Master of Science

Grand Forks, North Dakota

May
2018

This thesis, submitted by Benjamin W. McGee in partial fulfillment of the requirements for the Degree of Master of Science from the University of North Dakota, has been read by the Faculty Advisory Committee under whom the work has been done and is hereby approved.

_____
Dr. Michael J. Gaffey, Committee Chair

_____
Dr. Sherwin J. Gormly, Committee Member

_____
Dr. Sherry K. Fieber-Beyer, Committee Member

This thesis is being submitted by the appointed advisory committee as having met all of the requirements of the School of Graduate Studies at the University of North Dakota and is hereby approved.

_____
Grant McGimpsey
Dean of the School of Graduate Studies

_____
Date

PERMISSION

Title	Determining the correlation significance between S-type asteroid orbital inclination and albedo attributable to space weathering
Department	Space Studies
Degree	Master of Science

In presenting this thesis in partial fulfillment of the requirements for a graduate degree from the University of North Dakota, I agree that the library of this University shall make it freely available for inspection. I further agree that permission for extensive copying for scholarly purposes may be granted by the professor who supervised my thesis work or, in his absence, by the Chairperson of the department or the dean of the School of Graduate Studies. It is understood that any copying or publication or other use of this thesis or part thereof for financial gain shall not be allowed without my written permission. It is also understood that due recognition shall be given to me and to the University of North Dakota in any scholarly use which may be made of any material in my thesis.

Benjamin W. McGee
May, 2018

TABLE OF CONTENTS

LIST OF FIGURES

LIST OF TABLES

ACKNOWLEDGEMENTS

I would like to express my sincere gratitude to Dr. Michael Gaffey for supporting this research and affording me the opportunity to explore the intriguing realm located at the intersection of planetary geology and radiological engineering (and for guiding me along the way). Additionally, I would like to acknowledge the unwavering support of friend and mentor Dr. Sherwin Gormly, without whose sage advice I might have tumbled unknowingly into more than a few pitfalls – metaphorical and actual. To my parents, I hope to do justice to your steadfast faith in my abilities. Finally, to my wife and best friend, Jordan, I will forever remain indebted to you for your unflinching efforts both on my behalf as well as our children's while I whittled away at this, at times esoteric, undertaking; I am truly lucky that you understand I was born with my head above the clouds.

ABBREVIATIONS, ACRONYMS AND PREFIXES

AU	–	astronomical unit
BAR	–	Band Area Ratio
c	–	centi-
cm^{-3}	–	per cubic centimeter
CME	–	coronal mass ejection
eV	–	electron-volt
g	–	gram
G	–	giga-
GCR	–	galactic cosmic ray
k	–	kilo-
IMF	–	interplanetary magnetic field
m	–	meter
μ	–	micro-
n	–	nano-
NEA	–	Near-Earth Asteroid
NIR	–	near-infrared
PC	–	principal component
PCA	–	principal component analysis
s	–	second
SEP	–	solar energetic proton
SMASS	–	Small Main-belt Asteroid Spectroscopy Survey
SPE	–	Solar Particle Event
UV	–	ultraviolet

ABSTRACT

Recent research suggests that ion bombardment is more effective than micrometeoroid bombardment in albedo darkening of mature lunar soils, whereas micrometeoroid bombardment may act on longer timescales and is more effective in modifying the spectral features of a surface. This, in turn, may be extrapolated to suggest the following: 1) Increased intensities of ion bombardment would correlate negatively with the surface reflectivity of airless, silicate-bearing bodies known to express lunar-style space weathering, such as S-type asteroids, and 2) beyond that of sputtering and ion implantation, there is a gradient of potential interactions between the two weathering processes that may be relevant to space weathering at large, where via the processes of mineral metamictization and structural weakening, ion bombardment may act as a necessary precursor to micrometeroid bombardment in lunar-style space weathering. Because heliosphere research (i.e., the Ulysses spacecraft) reveals that the speed of solar wind rises with solar latitude from the equatorial plane to the poles, the possibility of a correlation is suggested between the albedo of a given S-type asteroid surface and its orbital inclination. In other words, more highly-inclined asteroids would be exposed to higher-intensity solar ion bombardment, which would thereby result in darker (or more quickly darkened) mature surfaces. This proposition is explored via the statistical analysis of a sample group of S-complex airless bodies, resulting in a statistically-significant negative correlation between orbital inclination and albedo at the 75% confidence level. An overall space-weathering scheme is proposed, and implications for space weathering mechanisms as they relate to orbital parameters are discussed.

1.0 INTRODUCTION

The exposed surfaces of asteroids and other airless bodies in the Solar System experience abstruse forms of geophysical weathering that can act to affect both an object's reflectivity (albedo) as well as its spectral signature (Hendrix and Vilas, 2006). Known generally as, "space weathering," the overall process has been considered a persistent complicating factor in the remote sensing of asteroid and planetary mineralogy and is believed to be typified (with notable exceptions) by the sort of weathering seen on the lunar surface, which expresses in the ultraviolet-visible-near-infrared (UV-vis-NIR) range from 0.2-2.7 μm as overall darkening, a reduction in the intensity of silicate mineral absorption bands, and an increase in spectral slope toward longer wavelengths, i.e., spectral reddening (Adams and McCord, 1971). This has been demonstrated over time to relate to nanophase iron entrained within a thin glass patina on exposed lunar regolith grains (Pieters et al., 2000). Research into the processes of space weathering has been driven in large part as a result of what is referred to as the "S-asteroid/ordinary chondrite conundrum," which references the fact that the spectra of the most common type of inner Main Belt asteroids (S-types) and the most common type of meteorites (ordinary chondrites) do not agree (Bell et al., 1989). While space weathering has been classically viewed as a process limited to airless body soil or regolith, ample evidence exists that space weathering operates on exposed rock as well (Noble, et al., 2011).

Despite the fact that space weathering has been linked both to ionizing radiation exposure as well as micrometeoroid impacts (Hapke, 2001) and has been studied in some detail on several airless bodies in the solar system, (e.g., on the Moon, Mercury, 243 Ida, 433 Eros, 25143

Itokawa, 6 Hebe, 4 Vesta), determining precisely how space weathering operates has proven an elusive goal. Space weathering effects vary dramatically between similar asteroids that would otherwise be expected to experience similar space weathering (Gaffey, 2010), and space weathering effects have been reportedly difficult to reproduce under laboratory conditions in a consistent way (Hemingway et al., 2015). Additionally, while it has been demonstrated that a parametric approach to the remote sensing of asteroid composition utilizing band centers and area ratios can "see through" space weathering effects to enable a corrected view of underlying mineralogy (Gaffey, 2010), a definitive space-weathering paradigm that successfully predicts the weathering effects observed across the Solar System has yet to be formalized. One possible solution to these discrepancies takes the form of an admission that space weathering results not from a single mechanism but is instead the result of a complex interrelationship between solar, mineralogical, orbital, and other airless body characteristics, the proper identification of which will be critical in untangling space weathering as a whole. This sentiment was converted succinctly by Thomas et al. (2014) into a justification for research when they declared that assessing the combination of measured characteristics, "can increase the scientific return beyond that of the individual datasets."

Therefore, it is sensible to review what are believed to be the primary two space weathering contributors (ion and micrometeoroid bombardment), explore potential interrelationships between ionizing radiation exposure and other potential space weathering processes, and examine space weathering effects in the context of previously-unconsidered asteroid orbital parameters. In this way, a refined understanding of space weathering and its drivers may be produced, with an eye toward identifying obscured trends and consequent areas of future potential research.

2.0 BACKGROUND

In order to fully explore the aspects of space weathering relevant to this work, it is necessary to establish a working knowledge of the fundamental physical characteristics of the target material (S-type asteroids), the space radiation environment and the heliosphere, and the effects of charged particles on the physical properties of materials. Respectively, these topics are briefly reviewed.

2.1. S-TYPE ASTEROID COMPOSITION AND TAXONOMY

The S-type asteroids are compositionally typified as iron and magnesium silicates and are most commonly found between 2 and 3 astronomical units (AU) from the Sun. Absorption band analyses have revealed that the S group is compositionally diverse, likely including both chondritic and achondritic bodies and representing in a majority of cases differing proportions of olivine and pyroxene, which serve to control observed spectral features (Gaffey et al., 1993). Specifically, S-type asteroid mineralogies range from dunites (pure olivine) through that of ordinary chondrites to nearly pure orthopyroxenes.

Because only very few S-type asteroids have been visited by spacecraft in order to obtain high-resolution imagery, the primary remote-sensing technique for determining the composition of S-types are diagnostic absorption features in reflectance spectra associated with the presence of crystalline olivine and pyroxenes; these include a three-band composite absorption feature for olivine centered roughly at 1 μm, and two absorption features for pyroxenes, with one absorption band centered approximately at 1 μm, referred to as "Band I," and the other centered at 2 μm, referred to as "Band II" (Cloutis et al.,1986). These are caused by the presence of Fe^{2+} in the

crystal matrix. Usefully, the positions of each band are also olivine-and-pyroxene-sensitive. For example, an increasing Band I center correlates to an increasing presence of olivine. Further, the combination of these Band I and Band II absorption features (the ratio of the area of Band II to the area of Band I) have been related to the abundances of pyroxene and olivine, known as the Band Area Ratio, or BAR.

For the purposes of this analysis, the Small Main-Belt Asteroid Spectroscopic Survey (SMASS) Phase-II classification scheme for asteroid taxonomy is employed (Bus & Binzel, 2002). The SMASS scheme is similar in initial form to the earlier Tholen (1989) classification scheme, which was created by combining reflectance spectra and albedo data to arrive at a general discrimination of asteroids by presumed mineralogical composition. The Tholen classification, itself built upon the older taxonomy proposition by Chapman et al. (1975), established what is arguably the most frequently-referenced classes of asteroids: carbonaceous (C), silicaceous (S), and X-types (which are often generalized as metallic, or M-type asteroids). However, unlike Tholen's work, the SMASS taxonomy did not consider object albedo in its methodology, relying instead on features revealed by high-resolution reflectance spectra. This is the driving distinction in the context of the present work, given that asteroid albedo is the dependent variable under consideration (see Sections 5.0 and 6.0).

Specifically, the SMASS effort resulted in the spectral discrimination of several S-group types that are inferred to be mineralogically distinct from the main S-type. This taxonomy preserved previously-identified taxonomic classes, such as A, Q, and R-types (Tholen, 1984), which each possess moderate to deep 1-μm (Band I) absorption features, while adding K and L-types, which possess shallow 1-μm bands. Additionally, the SMASS classification was able to further resolve possible transitional spectral types within the standard S-type complex, classified

as Sa, Sk, Sl, Sq, and Sr. The spectral zones for these subtypes are presented in Figure 1 (adapted from Bus & Binzel, 2002).

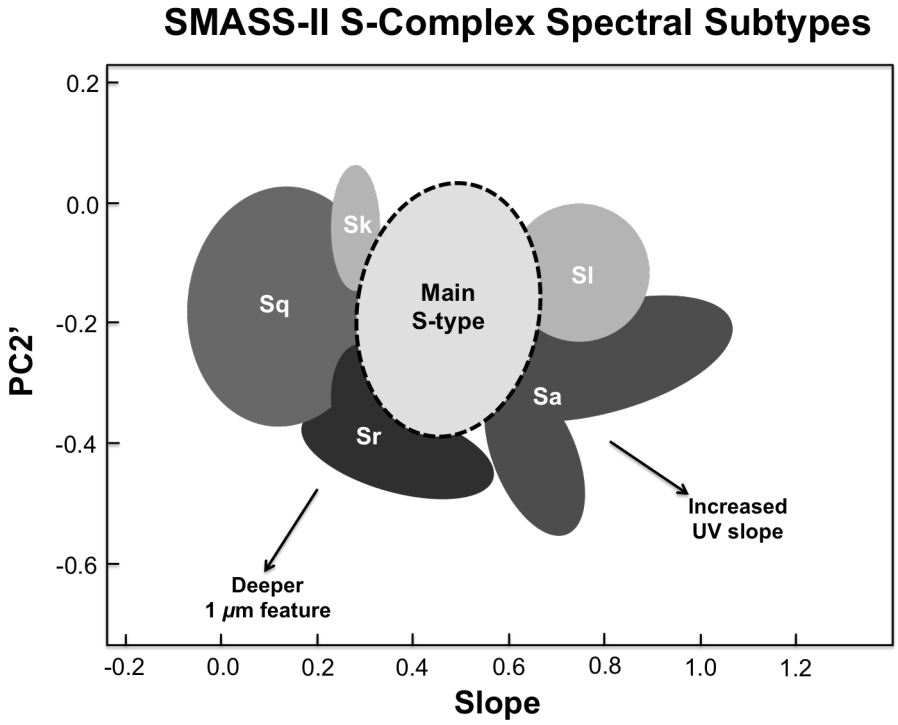

Figure 1. Spectral component plot for the S-type asteroid complex

This figure illustrates transitional S-subtypes (modified from Bus & Binzel, 2002). Parameterization of the spectral data was achieved via principal component analysis (PCA) according to Tholen (1984). Accordingly, PC2' is plotted on the vertical axis and refers to the second-largest fraction in dataset variance, which in this case is sensitive to the depth of the 1-μm absorption band (silicate indicator); "Slope," on the horizontal axis, refers to the object's normalized spectral slope.

Due to the possibility that these subtypes are either compositionally distinguishable from the main S-type or represent a gradient between weathered and unweathered surfaces of the same type (see Q-type discussion, below), they in either case potentially provide an opportunity to evaluate specific S-type weathering effects. Especially considering that unweathered olivine tends to be more reflective than pyroxene, it is possible that parallel weathering trends might be

elucidated in subgroups with varying mineral abundances, empirically pointing toward underlying "native" albedos that may differ due to variations in intrinsic mineralogy. To this end, the prospective mineralogical distinctions between the Sk, Sl, Sq, and S subtypes are briefly reviewed below[1].

The Sk-subtype is transitional with the K-type asteroids, which are themselves typified as being low albedo (~0.09) and spectrally similar to primitive CV/CO-type chondrites (Bell, 1988). The Sl-subtype, by contrast, has been typified by spectral similarity to differentiated ureilites (Dunn et al., 2013), which possess a slightly higher albedo (~0.18) but relatively flat reflectance spectra. Being spectrally similar to LL-type chondrites (Dunn et al., 2013), the Sq-subtype is transitional between S-type and Q-type asteroids, which have a slightly higher-still albedo (~0.20) and bear the greatest similarities to ordinary chondrites than any other asteroid class. In fact, some have suggested that core S-types are simply Q-types that have undergone space weathering and are regarded as a potential key to the resolution of the ordinary chondrite conundrum[2]. Lastly, the Sr-subtype, being spectrally similar in several cases to primitive achondrites as well as to basaltic achondrites, are transitional to the R-type asteroids, which are relatively-bright albedo bodies (~0.384) with strong olivine and pyroxene absorption features (Majess et al., 2008).

2.2. THE NOMINAL SOLAR SYSTEM MICROMETEOROID (DUST) ENVIRONMENT

In situ data recorded by two spacecraft largely inform the present understanding of the ambient micrometeoroid (i.e., dust) environment in the interplanetary space of the inner Solar

[1] The Sa-subtype is omitted here, as no bodies of this subtype are present within the population of the present study.

[2] Binzel et al. (2004) present a statistical size-distribution argument that at diameters greater than 5 kilometers, regolith production and evolution quickly react to space weathering processes, modifying the surfaces of Q-type asteroids to S-types.

System, those being the Galileo and Ulysses spacecraft; the two craft used identical instrumentation to record dust impacts across the inner solar system along their interplanetary trajectories, which were either largely parallel to or almost perpendicular to the Solar System's invariant plane, respectively (Grun et al., 1992a; Grun et al., 1992b). The orbital trajectories are presented in Figure 2 (adapted from Grun et al., 1997).

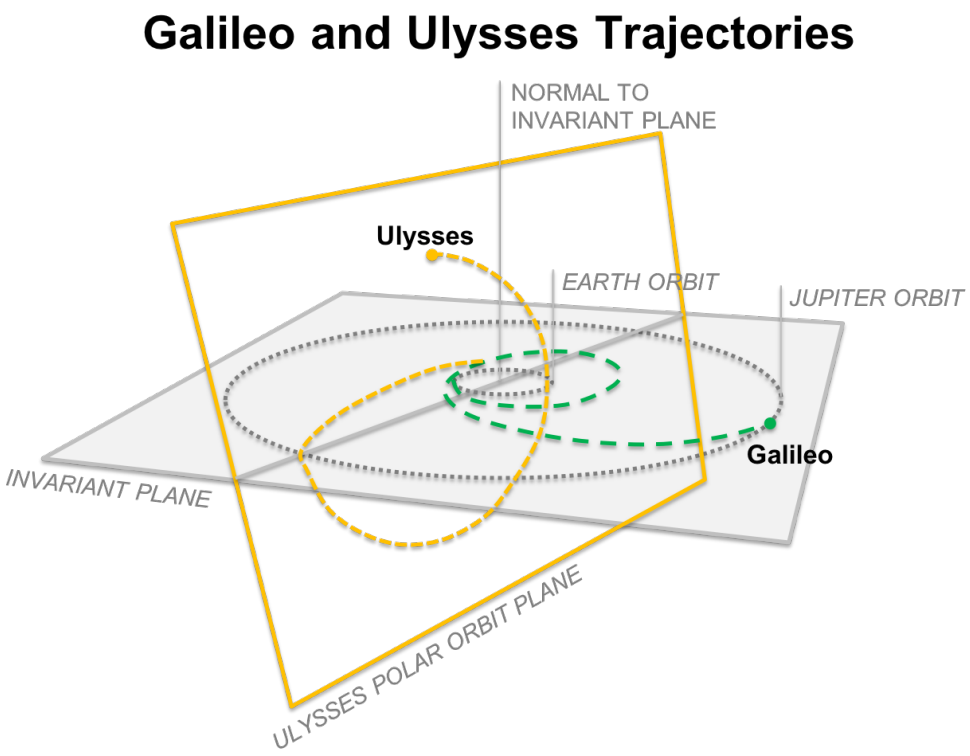

Figure 2. Trajectories of the Galileo (dashed, green) and Ulysses (dashed, yellow) spacecraft

The Sun is at the center, with the Earth, Jupiter, and Galileo trajectories within the Solar System invariant plane (shaded). The first portion of the Ulysses craft's trajectory was also in the plane of the ecliptic, until a Jupiter encounter was used to move the craft to a high-inclination orbit of 79 degrees.

By combining the datasets produced by these two spacecraft, a rough understanding of the overall latitudinal and radial distributions of micrometeoroids is produced (Grun et al., 1997). Specifically, the inner Solar System dust was found to be composed of at least two distinct types.

The first, interplanetary dust, was found to possesses grains with a wide range of masses (from 10^{-16} to 10^{-6} grams, g) that are located at "low" inclinations nearer to the plane of the ecliptic (i.e., heliospheric latitudes below 30 degrees). The second general type, referred to as interstellar dust, was found to be composed of grains with a narrower range of smaller masses (from 10^{-14} to 10^{-12} g), located at "high" inclinations and ecliptic latitudes (i.e., heliospheric latitudes greater than 50 degrees). Simultaneously, Ulysses data revealed that the micrometeroid impact rate averaged as low as 0.3 impacts per day at high ecliptic latitudes, whereas within the ecliptic plane, the impact rate rose to up to 1.5 impacts per day (Kruger et al., 2010). The overall relationship between dust density at a given heliographic latitude and the inclination of orbiting dust is governed by Equation 1, below, which establishes the (perhaps intuitive) reality that in order for a micrometeoroid to reach a given heliographic latitude, its solar orbital inclination must be at least that large (modified from Grun et al., 1997):

$$i \geq \lambda \qquad (1)$$

Further, the lowest-mass particles were also generally found to be the fastest, with the high-inclination, 10^{-14} to 10^{-12} g mass band having velocities from 5-11 kilometers per second (km/s), and the low-inclination, 10^{-16} to 10^{-6} g ecliptic dust having velocities from 2-45 km/s, with an overall average value of 20 km/s (Kruger et al., 2010). This yields the reality that high-inclination micrometeoroid impacts appear five times less likely than impacts within the ecliptic plane, and on average, high-inclination micrometeoroid strikes are generally less massive and less energetic than their ecliptic counterparts.

2.3. THE NOMINAL SOLAR SYSTEM IONIZING RADIATION ENVIRONMENT

The ambient environment of the Solar System is typified by a dynamic mix of charged particles (ions) originating from multiple high-energy sources that are local, galactic, or extra-galactic in origin (Tribble, 2003). These sources include the Sun, other stars in the Milky Way, galactic processes (e.g., galactic cores), and interactions of the particles produced by these sources with the surfaces (and atmospheres) of celestial bodies, which produce secondary radiation (e.g., albedo neutrons).

Of these multiple radiation sources, particles continuously emitted by the Sun dominate the Solar System's radiation environment by number. This so-called "solar wind" results from the supersonic expansion of the outer atmosphere of the sun, or solar corona, and is composed predominantly of ionized hydrogen (~95%), with trace contributions of ionized helium (~5%) and heavier elements (~0.1%) (Killen et al., 2012). Due to the fact that interplanetary space is dominated by these charged particles produced by the Sun, the regions of space filled by the solar wind have been described as the "heliospheric medium" (Balogh et al., 2001). The solar magnetic field interacts with and spatially moderates this expanding, hot material, which is ejected from the Sun with velocities ranging from 250 to greater than 800 kilometers per second (km/s) for "slow" and "fast" solar wind, respectively (Gosling & Pizzo, 1999; Durante & Cucinotta, 2011).[3] An average speed in the plane of the ecliptic of 400 km/s is often used to represent generalized solar wind (Killen et al., 2012). While many researchers cite average solar wind proton energies of a thousand electron-volts (1,000 eV, or 1 keV) over long timescales for the purposes of solar wind simulations and modeling (e.g., Starkuhina, 2006), these slow and fast solar wind velocities equate to average proton particle energies ranging from 100 eV to

[3] During Solar Particle Events (SPEs), such as coronal mass ejections, the speed of emitted solar wind can more than double when compared with nominal values, while the solar wind ion density can grow by a factor of 10.

approximately 3.5 keV (Durante & Cucinotta, 2011). Likewise, while an average proton particle density value of 5 per cubic centimeter (cm^{-3}) is also often used to represent generalized solar wind (e.g., Killen et al., 2012), the average slow wind particle density is in actuality closer to 11 cm^{-3}, while the fast solar wind particle density is closer to 3 cm^{-3}, nearly an order of magnitude lower (Balogh et al., 2001). Note also that these nominal values are punctuated by episodic Solar Particle Events, which lead to bursts of coronal protons with particle energies up to more than a billion electron volts (GeV).

In contrast to solar wind, so-called Galactic Cosmic Rays, or GCRs, (a legacy misnomer referring to interstellar ions), are orders of magnitude fewer in number than solar wind particles, arrive to the Solar System isotropically, but dominate in terms of particle energies – up to GeV intensities and higher. This is owing to the fact that GCRs result from much more energetic processes (e.g., supernovae). It is also particularly noteworthy that these two particle fields (solar wind and GCRs) are inversely related to one another. Because the solar wind acts as a carrier for the Sun's magnetic field through interplanetary space, increased solar activity strengthens the interplanetary magnetic field (IMF) and attenuates arriving GCRs. Likewise, periods of reduced solar activity correlate to an increase in the number and energy of arriving GCRs able to penetrate deep into the inner Solar System. However, due to the overall reduced GCR flux when compared to the solar wind, it is solar wind that is considered to be the mechanism of primary concern with respect to ion bombardment and space weathering.

2.4. THE HELIOSPHERE

While the average values described in Section 2.3 are commonly employed when modeling solar ion bombardment across geologic timescales, it is worth noting that the heliosphere is dynamic, with nontrivial variations based on period in the Solar Cycle and

distance from the invariant plane of the Solar System. For example, the relationship between the energy of the heliospheric medium (solar wind) and heliographic latitude is an important one, particularly regarding the potential role(s) of ion bombardment in space weathering processes. Consequently, when seeking to describe the principal characteristics of the heliospheric medium with respect to space weathering, there are three relevant factors to consider.

2.4.1. SOLAR WIND ENERGY HELIOGRAPHIC LATITUDE DEPENDENCE

First, the Sun expresses a sharp, bimodal latitude dependence of solar wind speeds during Solar Minimum (Suess, 1999). During this time, so-called "slow" solar wind speeds are found in the solar equatorial plane, which is approximately aligned with the plane of the ecliptic. Governed by the IMF and the solar current sheet in this region, this radiation possesses speeds of approximately 300-400 km/s (~100 eV) and is organized by closed, near-surface magnetic structures into a band or "streamer belt" aligned with the Sun's magnetic equator. The transition from slow to so-called "fast" solar wind under these conditions occurs at approximately ±15 degrees heliographic latitude and may extend to ±25 degrees (Balogh et al., 2008), though the transitions are also measured to be abrupt – as sharp as 1.5 degrees in span. The fast wind remains relatively constant from the terminus of this transition zone to the solar poles, where the solar wind possesses speeds of greater than 800 km/s (~3.5 keV). This fast solar wind is generated by the open magnetic field structure aligned with the axis of the Sun's magnetic dipole, generating regions known as polar "coronal holes." Traditionally, this general schematic of solar wind characteristics is used to represent the average ion bombardment environment for bodies in the Solar System, which implies that during and in proximity to Solar Minimum, airless bodies with more inclined orbits will experience more energetic ion bombardment than

bodies orbiting within or very near to the plane of the ecliptic. This heliographic latitude-dependence for solar wind energy is depicted in Figure 3.

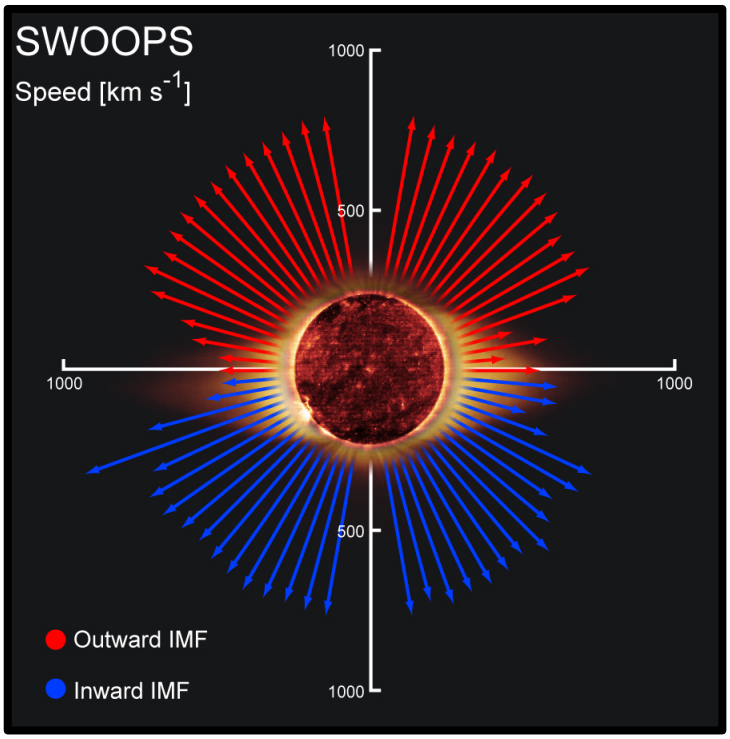

Figure 3. Radial plot of Solar Minimum solar wind speed as measured by the Ulysses spacecraft

Obtained by the Ulysses spacecraft SWOOPS sensor during Solar Minimum, which highlights slow wind at the solar equator and fast wind approaching the poles. Blue and red-colored lines represent the orientation and overall state of the solar magnetic dipole, which drives the IMF. (Image credit: ESA)

2.4.2. SOLAR AXIS OBLIQUITY

Secondly, the Sun's rotational axis possesses non-zero obliquity with respect to the angular momentum vector of the rest of the system of planets that orbit it. In other words, the Sun's axis of rotation is tilted from the invariant plane of the Solar System, with published values of the tilt of the Sun's equatorial plane ranging from 5.8 to 7.25 degrees (Heller, 1993; Balogh et al., 2001; Souami & Souchay, 2012; Bailey et al., 2016). Additionally, near Solar

Minimum, the magnetic dipole does not perfectly align with the rotation axis but is instead tilted with respect to it by tens of degrees (Balogh et al., 2008). This is illustrated in Figure 4.

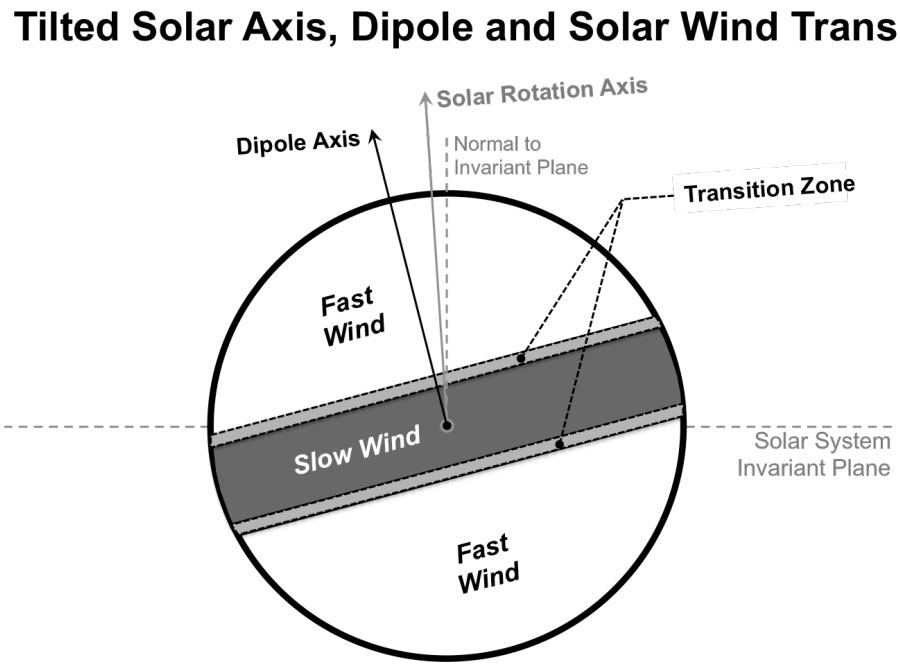

Figure 4. Diagram of the tilted solar dipole relative to the Sun's rotation axis

Modified after Pizzo (1991) to include the tilt of the solar rotation axis, this highlights the pattern of fast-slow solar wind interactions that would be experienced while orbiting the Sun, or while the Sun rotates, during an organized dipole state (i.e., Solar Minimum).

The implication of this obliquity on airless bodies with respect to the transition zone between slow and fast solar wind is non-trivial. At first glance, it may seem that the orbital inclination of a given airless body would be expected to correlate directly to positive and negative heliographic latitude of the same value, i.e., only objects with orbital inclinations inclined more severely than 15 degrees would be expected to experience any transitional or fast solar wind in the regions greater than ±15 degrees heliographic latitude. However, it becomes obvious when including solar obliquity and dipole tilt considerations that bodies with orbital

inclinations as low as 9 degrees could reach through the transition zone into the fast solar wind for a significant portion of their orbits.

To begin to understand these effects, the astrodynamics of an inclined orbiting body become particularly relevant as it relates to what may be considered the residence time, or fraction of each orbit, that a body spends at a given heliographic latitude. Generally-speaking, for an ideal, circular Kepler orbit about the Sun (or any other body), an orbiting object inclined less than 90 degrees spends the greatest amount of time near its "northernmost" and "southernmost" latitudes while spending the least amount of time near to the equator. Specifically, where i is an object's inclination and σ represents a heliographic latitude of interest, the fraction of time, f, spent in a given (heliographic) latitude is mathematically described by Equation 2, below (modified from Bate et al., 1971):

$$f(\sigma) = 1/\pi * \cos(\sigma) / (\sin^2 i - \sin^2\sigma)^{1/2} ; \ -i < \sigma < i \qquad (2)$$

Assuming a 7.25-degree solar obliquity (Balogh et al., 2001), all airless body orbital inclinations would consequently need to subtract 7.25 degrees to each the northern and southern extents in terms of heliographic latitude. For example, an airless body with an orbital inclination of 20 degrees actually orbits between 12.75 degrees north and 27.25 degrees south heliographic latitude. According to Equation 1 (assuming a circular orbit and no precessional motion), the object spends more than 40% of its orbit in the fastest solar wind in the southern latitudes. These fractions of an orbit might be considered a sort of "residence period" for any airless body spent exposed to fast solar wind. And while this example is not wholly realistic in terms of orbital parameters, the implication is that even if an airless body only grazes the fast solar wind by the numbers, based on orbital dynamics averaged over geologic time, it will in reality spend an appreciable portion of its orbital life being exposed to it.

2.4.3. PERIODIC SOLAR DIPOLE REORGANIZATION

Third, it is important to note that the solar magnetic dipole is generally not coherent nor aligned with the Sun's axis of rotation during Solar Maximum, at which time the field is chaotic and highly complex, with streamer belts and coronal holes observed at all latitudes. Figure 5 presents the solar wind radial plot observed by the Ulysses spacecraft during Solar Maximum.

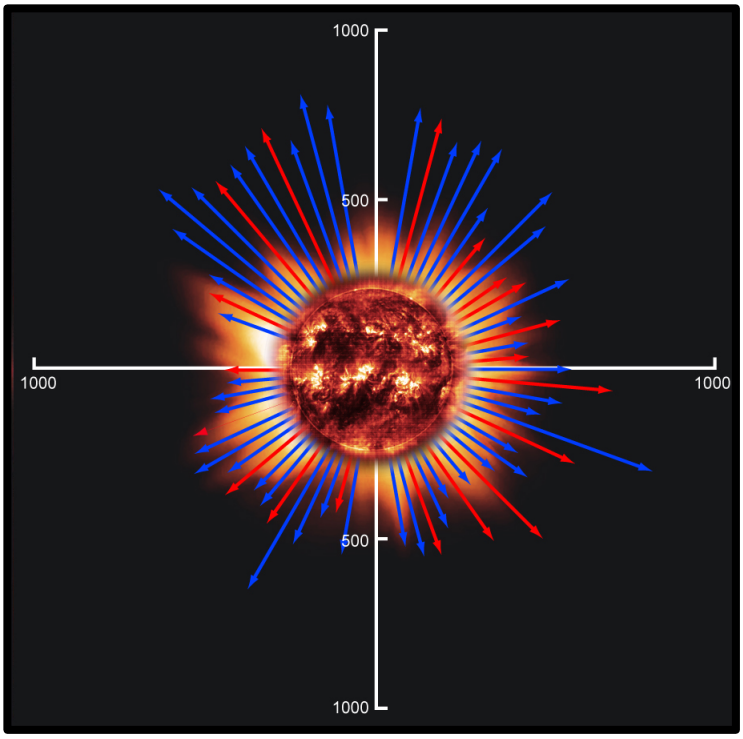

Figure 5. Radial plot of Solar Maximum solar wind speed as measured by the Ulysses spacecraft

Measured by the Ulysses spacecraft SWOOPS sensor during Solar Maximum, the figure highlights fast and slow winds at all latitudes, consistent with Solar Maximum activity. Scale (km per second) is identical to Figure 3. Blue and red-colored lines represent the orientation and overall state of the solar field and IMF. (Image credit: ESA)

Likewise, the field is increasingly coherent but strongly misaligned with the solar axis of rotation when leaving Solar Maximum and approaching Solar Minimum, a period known as the

"declining phase." Instead, during the declining phase, the solar dipole has been observed to be substantially inclined with rest to the axis of solar rotation (Gosling & Pizzo, 1999). Indeed, this dipole tilt has been measured to be as severe as 30 degrees with respect to the rotational axis before returning to a traditional equatorial-aligned orientation during the subsequent Solar Minimum (Suess et al., 1998). Figure 6 presents an illustration of this pattern across the Solar Cycle.

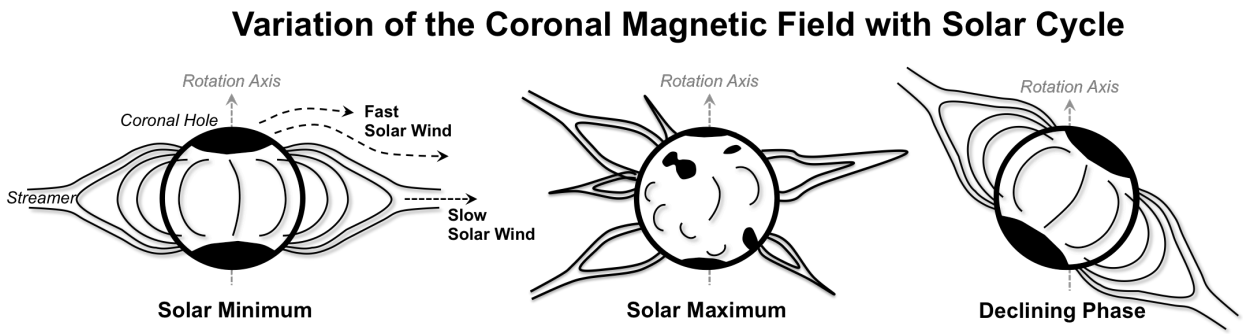

Figure 6. Diagram of the variation of the Solar Cycle coronal magnetic field

Patterned after the classic depiction by Suess et al. (1998), this figure illustrates from left to right the highly-organized dipole generally aligned with the rotation axis during Solar Minimum, the highly chaotic magnetic field during Solar Maximum, and the highly inclined solar dipole during the Declining Phase, respectively.

This reality greatly extends the apparent heliographic latitude of fast solar wind emission, which in turn regularly exposes a much wider range of objects with lower orbital inclinations to fast solar wind than would be expected given the more conventional view of the heliosphere presented in Section 2.3.1 and 2.3.2. However, as this exposure is cyclical, those bodies with inclinations exceeding the Solar Minimum fast-wind threshold heliographic latitudes would still be expected to be exposed to more fast wind than those in equatorial orbits, and so the Solar Maximum chaos and declining phase dipole inclination can arguably be ignored without jeopardizing the orbital inclination-solar wind dependence argument upon which the present

work relies. This in mind, it remains important to understand that a gross approximation is being made when generalizing fast and slow solar windspeeds as being in organized heliographic latitude bands only observed during Solar Minimum.

2.5. ION BOMBARDMENT AND MINERAL AMORPHIZATION/WEAKENING

In literature concerning space weathering, ion bombardment as a physical process tends to emphasize "sputtering" as a primary weathering mechanism (e.g., Rodriguez-Nieva et al., 2011). This describes the process of recoil particles being ejected from an incident surface in response to ion collisions, with focus drawn more to the availability of freed particles to interact as part of the weathering process than to the remnant effect on the material from which the particle was freed. However, the bombardment of surficial materials with any ion of sufficient energy to cause atomic displacements within a crystal lattice can result in further, significant microstructural changes to the material's molecular/mineral structures, e.g., mineral amorphization, point defects, and solute aggregates (Zinkle, 2012). It has even been shown that a lone heavy ion can form a nanometer-scale crater on the surface of a material if it is possessive of impact energies equal to or greater than 5 keV, blurring the distinction between micrometeoroid impact ejecta and incident bombarding ion sputtering (Djurabekova et al., 2012). These structural changes have been shown to significantly change physical and mechanical properties of affected materials, making them more susceptible to further degradation via secondary processes[4]. Specifically, depending on overall dose delivered, the changes in an irradiated material's physical and mechanical properties include the induction of crystalline-to-

[4] This is a subject of great interest to manufacturers of materials subject to regular bombardment by proximal nuclear reactors or ion accelerators, which forms a bulk driver for research in this area. In the case of the former, hydrogen embrittlement acts in concert with structural embrittlement and damage to the alloys composing reactor containment vessels. In the case of the latter, the build-up of electric fields in a vacuum leads to plasma-escape ions that damage containment walls.

amorphous phase transitions due to the ion collision sequence's ionization cascades. This can cause material swelling of 5-30% by volume as well as a reduction in the material's elastic modulus; also, the so-called "hardening" of the material matrix may occur, which for many materials is correlated with a lowered fracture toughness (Zinkle, 2012). Both of these effects would result in the overall weakening of an irradiated material. Figure 7 presents a generalized diagram of these ion bombardment effects.

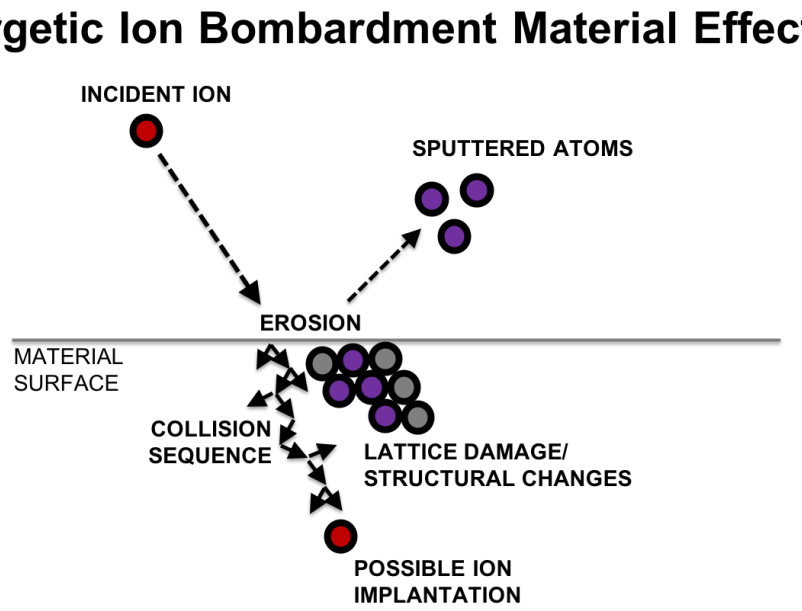

Figure 7. Generalized energetic ion bombardment material effects

Adapted from Kuhlman et al. (2015), this figure presents a generalized depiction of the material effects initiated by energetic ion bombardment, depicted in red. These include sputtering from the surface (in purple), surficial erosion, damage to the near-surface mineral structure, i.e., amorphization (in purple), lattice displacements and defects along the ion collision sequence (in purple), and ion implantation.

For example, consider that the typical threshold energy necessary to cause a single atomic displacement from a crystal lattice is 30-50 eV (Zinkle, 2012). In this case, even a low-speed-solar-wind proton (with an energy equivalent of 100 eV) possesses enough energy to displace

two atoms from a mineral crystal lattice per collision. Likewise, a fast-solar-wind proton (~ 3.5 keV) has the potential to displace on the order of 175 atoms per interaction. With an average areal irradiation rate of 5 ions impacting per square centimeter per second (cm^{-2} s^{-1}), for slow solar wind this equates to more than 300 million atomic displacements per square centimeter per year (cm^{-2} yr^{-1}) in an asteroid's outermost surface material, while for fast solar wind this equates to nearly 30 billion atomic displacements cm^{-2} yr^{-1}, a nontrivial difference of nearly two orders of magnitude. In each of these cases, research indicates that a fraction of each displacement cascade remains in clusters of non-correct but stable positions, i.e., that stable defects are created within the material's molecular framework. These defects are known to manifest in the presence of anisotropic crystal habit planes as the irradiation-induced growth and/or creep of individual crystal grains, which creates large grain-boundary stresses in polycrystalline materials. This, in turn, results in the loss of material strength described above as well as in grain boundary fractures at the macroscopic level (Zinkle, 2012).

In a broad sense, this may all be generalized as radiation-induced weakening and potential embrittlement of a material. While this weakening itself cannot cause the formation of nanophase-iron-entrained space-patina, it certainly appears plausible that such a process could enable or enhance a secondary process, such as micrometeorite impacts, to do so.

3.0 PURPOSE

The primary purpose of this study is to determine the direction and degree of correlation or association between the albedo of a representative population of S-type airless bodies (asteroids) and their respective orbital inclinations, which relates to the overall intensity of heliospheric medium (solar wind) exposure, where "intensity" refers to energy, a function of inclination, as opposed to overall flux, which is a function of semi-major axis. Consequently, the specific purpose of this work is to 1) test the null hypothesis that there is no statistically-significant linear association between the variables of albedo and orbital inclination for the target population of S-type asteroids when analyzed in bulk as well as by associated subtypes and orbit type, 2) analyze the covariance of the albedo-inclination regression lines for each of the S-subtypes, and 3) utilize the information derived from the primary investigation to hypothesize a weathering process, either as a single mechanism or combination of separate mechanisms, that accounts for the apparently contradictory expressions of space weathering observed amongst S-type asteroids.

4.0 STATEMENT OF THE PROBLEM

Conflicting expressions of space weathering persist on airless bodies of similar composition and distance from the Sun. On the mature surfaces of S-type asteroids, these expressions include the lowering of surface reflectivity (albedo) without a modification of spectral features, the modification of spectral features without affecting albedo, or combinations of both effects (i.e., approximating lunar-style space weathering). To date, the precise mechanism or interaction of mechanisms necessary to produce these weathering effects has not been identified but has been demonstrated to relate to at least two primary processes: ion bombardment and micrometeoroid bombardment. It is sensible, then, to pursue work intended to discriminate the effects of these processes based on other parameters, e.g., orbital characteristics.

5.0 SCOPE

The scope of this study is to statistically analyze two variables, albedo and orbital inclination, for a target population limited to the S-type asteroids for which suitable orbital, albedo, and compositional information is available. This necessarily restricts the study population to a collection of Near-Earth Asteroids (NEAs) and one Mars-Crossing Asteroid (1992 AX). The product of this work will be the degree of significance of correlation between the two variables for the total target population, several subsets of the total population, and the degree of covariance of the regression lines for the population subsets.

The data considered in this effort is derived from two sources. First, visible wavelength spectra for near-Earth and Mars-crossing S-type bodies were obtained as part of Phase II of the SMASS study (which includes published orbital parameters). Secondly, albedo measurements were obtained from the Spitzer near-Earth object survey (i.e., Harris et al, 2011; Mueller et al., 2011; Trilling et al., 2010; Thomas et al., 2011; Thomas et al., 2014), which were cross-referenced with the SMASS-II population to produce a total of 71 target S-type bodies with albedo information and each with a spectral classification as either a generic S-type object or one of the sub-types Sk, Sl, Sq, or Sr (Binzel et al, 2004)[5]. This dataset is included as Table 1, below. The dataset is also plotted as Figure 8a, below, which depicts the bodies under study in principal spectral component space, in the manner after Bus & Binzel (2002).

[5] In employing a method reliant only on spectra, it was recognized that the use of SMASS classifications as a proxy for general mineralogy in this inclination-albedo study preempts a corruption problem possible with other datasets where albedo was also used to derive asteroid classification information.

Table 1 – Asteroid information used in the present study

Asteroid Number	Asteroid Name	Provisional Designation	Orbit Type	SMASS Type	Inclination (degrees)	Albedo	Albedo Error (+)	Albedo Error (-)
433	Eros	1898 DQ	AMO	S	10.8	0.23	-	-
1627	Ivar	1929 SH	AMO	S	8.5	0.09	0.12	0.05
1685	Toro	1948 OA	APO	S	9.4	0.327	0.08	-
1865	Cerberus	1971 UA	APO	S	16.1	0.5	0.29	0.21
1866	Sisyphus	1972 XA	APO	S	41.2	0.07	0.09	0.04
7977	-	1977 QQ5	AMO	S	25.2	0.06	0.06	0.03
3122	Florence	1981 ET3	AMO	S	22.2	0.21	0.20	0.10
4957	Brucemurray	1990 XJ	AMO	S	35	0.18	-	-
7822	-	1991 CS	APO	S	37.1	0.28	0.18	0.12
15745	Yuliya	1991 PM5	AMO	S	14.4	0.24	0.18	0.11
6047	-	1991 TB1	APO	S	23.5	0.8	0.44	0.35
6455	-	1992 HE	APO	S	37.3	0.31	0.42	0.18
32906	-	1994 RH	AMO	S	18.9	0.14	0.11	0.08
13651	-	1997 BR	APO	S	17.2	0.34	0.29	0.21
16834	-	1997 WU22	APO	S	16	0.43	0.28	0.20
100756	-	1998 FM5	AMO	S	11.5	0.26	0.19	0.14
100926	-	1998 MQ	AMO	S	24.2	0.37	0.22	0.16
85818	-	1998 XM4	APO	S	62.7	0.3	0.23	0.15
85953	-	1999 FK21	ATE	S	12.6	0.076	0.05	0.04
86326	-	1999 WK13	AMO	S	34.3	0.27	0.21	0.12
357022	-	1999 YG3	APO	S	34.5	0.18	0.14	0.08
18882	-	1999 YN4	AMO	S	36.8	0.18	0.15	0.09
20790	-	2000 SE45	AMO	S	8.3	0.1	0.11	0.05
-	-	2000 YF29	APO	S	6.3	0.27	0.16	0.11
54686	-	2001 DU8	AMO	S	33.2	0.35	-	-
200840	-	2001 XN254	AMO	S	1.9	0.65	0.26	0.28
-	-	2002 AQ2	AMO	S	11.7	0.2	0.12	0.10
10115	-	1992 SK	APO	S	15.3	0.38	0.24	0.17
96590	-	1998 XB	ATE	S	13.6	0.11	0.09	0.05
208023	-	1999 AQ10	ATE	S	6.5	0.46	0.25	0.22
12923	Zephyr	1999 GK4	APO	S	5.3	0.2	0.16	0.09
22099	-	2000 EX106	APO	S	9.8	0.29	0.16	0.12
285540	-	2000 GU127	APO	S	8.5	0.32	0.18	0.16
25143	Itokawa	1998 SF36	APO	S	1.6	0.41	0.20	0.18
35107	-	1991 VH	APO	Sk	13.9	0.26	0.20	0.11
5407	-	1992 AX	MCA	Sk	11.4	0.199	0.08	-
18736	-	1998 NU	AMO	Sk	2.8	0.25	0.19	0.14
162142	-	1998 VR	ATE	Sk	21.8	0.14	0.10	0.07
55532	-	2001 WG2	APO	Sk	38.5	0.14	0.12	0.06
1980	Tezcatlipoca	1950 LA	AMO	Sl	26.9	0.47	0.43	0.24
1917	Cuyo	1968 AA	AMO	Sl	23.9	0.27	0.21	0.14
137064	-	1998 WP5	AMO	Sl	19.5	0.29	0.25	0.14
54690	-	2001 EB	AMO	Sl	35.4	0.24	0.21	0.11
1863	Antinous	1948 EA	APO	Sq	18.4	0.11	0.08	0.05
4183	Cuno	1959 LM	APO	Sq	6.7	0.1	0.10	0.05

Asteroid Number	Asteroid Name	Provisional Designation	Orbit Type	SMASS Type	Inclination (degrees)	Albedo	Albedo Error (+)	Albedo Error (-)
2340	Hathor	1976 UA	ATE	Sq	5.9	0.6	0.28	0.21
2063	Bacchus	1977 HB	APO	Sq	9.4	0.27	0.21	0.16
4947	Ninkasi (large)	1988 TJ1	AMO	Sq	15.7	0.32	0.20	0.17
4947	Ninkasi (small)	1988 TJ1	AMO	Sq	15.7	0.5	0.29	0.25
99907	-	1989 VA	ATE	Sq	28.8	0.24	0.19	0.11
5587	-	1990 SB	AMO	Sq	18.1	0.29	0.43	0.19
6053	-	1993 BW3	AMO	Sq	21.6	0.069	0.10	0.05
7358	Oze	1995 YA3	AMO	Sq	4.7	0.08	0.10	0.04
344074	-	1997 UH9	ATE	Sq	25.5	0.36	0.23	0.15
175729	-	1998 BB10	APO	Sq	11.5	0.43	0.24	0.21
137062	-	1998 WM	APO	Sq	22.5	0.32	0.23	0.14
85938	-	1999 DJ4	APO	Sq	9.1	0.28	0.23	0.13
40267	-	1999 GJ4	APO	Sq	34.5	0.28	0.28	0.14
66959	-	1999 XO35	AMO	Sq	20.6	0.28	0.20	0.16
137799	-	1999 YB	AMO	Sq	6.8	0.31	0.21	0.17
203015	-	1999 YF3	AMO	Sq	26.8	0.19	0.14	0.11
36284	-	2000 DM8	APO	Sq	46.8	0.19	0.16	0.09
138258	-	2000 GD2	ATE	Sq	32.1	0.44	0.22	0.20
20826	-	2000 UV13	APO	Sq	31.9	0.18	0.31	0.12
141052	-	2001 XR1	APO	Sq	17.7	0.22	0.08	0.05
31346	-	1998 PB1	AMO	Sq	6	0.2	0.14	0.11
2062	Aten	1976 AA	ATE	Sr	18.9	0.2	-	-
12711	Tukmit	1991 BB	APO	Sr	38.5	0.19	0.14	0.09
16657	-	1993 UB	AMO	Sr	25	0.09	0.09	0.04
9400	-	1994 TW1	AMO	Sr	36	0.14	0.16	0.10
11398	-	1998 YP11	AMO	Sr	15	0.176	0.19	0.09

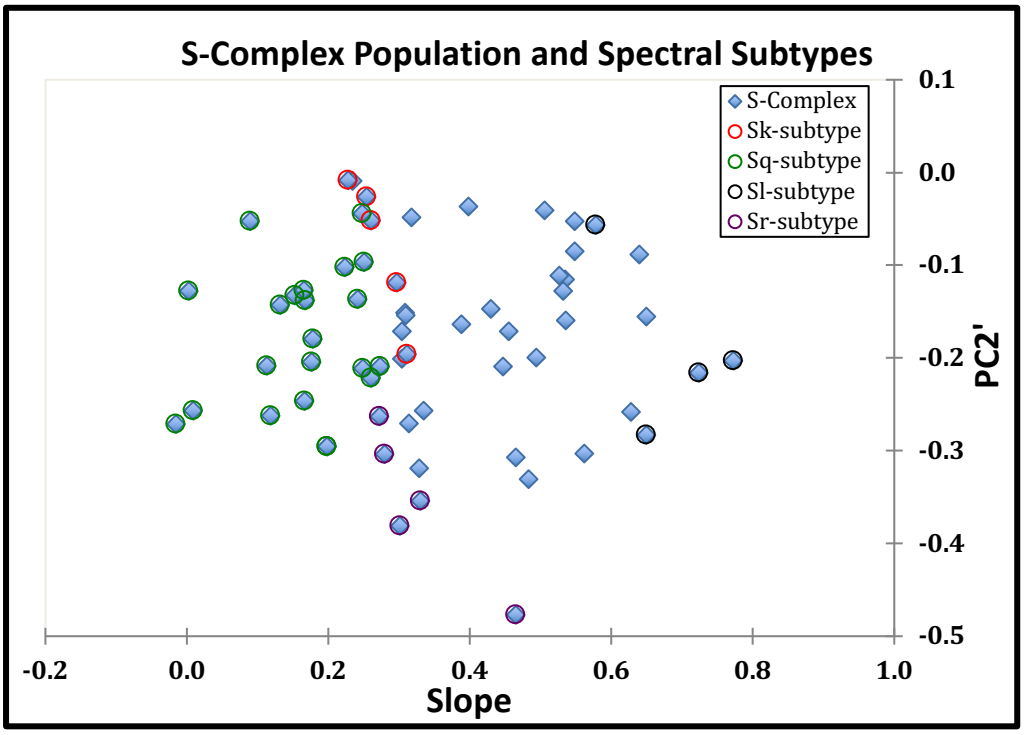

Figure 8. ***Spectral component plot for the present study S-type asteroid population***

Spectral component plot for the S-type asteroids included in this study, illustrating S-complex subtypes by plotting PC2' against normalized spectral slope, as in Bus & Binzel (2002). Compare to Figure 1, for reference.

6.0 METHODS

The proposed procedure is analytical in nature and centers on the statistical analyses of a set of S-type asteroids, airless bodies known as a class to experience varying styles of space weathering, whose compositional distinctions were discriminated based on a methodology that did not include measurements of albedo (i.e., SMASS-II, see: Bus & Binzel, 2002). The selection of this target population (refer to Section 5.0 for more information) is due to the fact that one of the two primary variables to be considered is itself asteroid albedo, referred to here as *y*, or the dependent variable. The other variable is asteroid orbital inclination, referred to here as *x*, or the independent variable. Nominative variables to be included in secondary analyses include asteroid type/subtype as well as NEA orbit type (i.e., Amor, Apollo, and Aten).

This asteroid population, included in Section 5.0 as Table 1, results in a total N value of 71. Organized by asteroid type and subtype, the first statistical test to be performed is to determine the direction and significance of the correlation coefficient, *r*, between albedo (*y*) and orbital inclination (*x*) for the target population and various subsets thereof. This takes the form of a linear (or Pearson), two-tailed correlation analysis between *x* and *y* in each case (S-type and subtype), where the null hypothesis is formulated as [-critical value] > *r* < [critical value], representing no statistical association between the variables; the alternative hypothesis therefore takes the form, [-critical value] < *r* > [critical value], representing a statistical association between the variables (Natrella, 2005). The second statistical evaluation to be performed is an analysis of covariance between the regression lines produced for the subtypes analyzed in the first analysis, which will compare a calculated P value, or the probability that given a true null

hypothesis for the observations would be produced, to an established significance level, *a*. Finally, as a form of cross-check against the primary evaluation, the last analysis to be performed is to determine the direction and significance of the correlation coefficient, *r*, between albedo (*y*) and orbital inclination (*x*) amongst the total target population organized not by SMASS subtype but rather by orbit type amongst the same population. This is in order to evaluate whether or not trending based on proposed "freshening" mechanisms is present in the dataset, and further, if any trends agree with the conceptual relationship to orbit type as described in Section 7.6.

Due to the small available sample size and the wide uncertainty in published albedo values, for the purposes of this study a significance level, *a*, of 0.25 was selected, which represents a 75% confidence level in the ability to potentially confirm or reject the null hypothesis based on the available data. In other words, the *a* of 0.25 implies that there is a 25% chance that any correlation observed that serves as a basis for rejecting the null hypothesis is not real and is instead an artifact of natural variability in the sample population, otherwise known as a Type I error. Considering the small sample size and high degree of potential intrinsic error for the population of asteroids under consideration, this level of risk is viewed by the author to be acceptable and the effort to identify possible or likely relationships.

For reference, the degrees of freedom for a two-tailed Pearson analysis, df, are equal to N-2. Accordingly, it follows that for the total selected population of S-complex asteroids in the present study, df = 69. Consequently, at the 75% confidence level, the critical value for the entire study population is ±0.1380, and so [$-0.1380 > r < 0.1380$] describes the statistical conditions under which the null hypothesis is confirmed, while [$-0.1380 < r > 0.1380$] describes the statistical conditions under which the null hypothesis is rejected and the alternative hypothesis is

confirmed. The full range of statistical parameters and criteria for the dataset are included as Table 2, below.

Table 2 – Statistical parameters/criteria for the target asteroid population

Asteroid Type	Sample Population (#)	Degrees of Freedom (df)	Significance Level (*a*)*	Critical *r*-value
S-total	71	69	0.25	0.1380
S-only	34	32	0.25	0.2028
Sk	5	3	0.25	0.6347
Sl	4	2	0.25	0.7500
Sq	23	21	0.25	0.2500
Sr	5	3	0.25	0.6347
Amor	32	30	0.25	0.2094
Apollo	29	27	0.25	0.2207
Aten	9	7	0.25	0.4284

Note: The divided rows represent data partitioning by subtype and by orbit type, respectively; the sum of the last group is one less than the total, which is due to the exclusion of one Mars-Crossing Asteroid in the population.

* The confidence level for the analyses to be performed on the target S-type asteroid population under study is 75%.

7.0 LITERATURE REVIEW

In establishing the current state of research relevant to the present work, a review of literature regarding space weathering mechanisms, space weathering on airless bodies in the Solar System, and a proposed anti-weathering process was performed. Additionally, an overall space weathering scheme patterned after the Hemingway et al. (2015) work on the Renier Gamma lunar anomaly was also suggested. Respectively, these topics are briefly reviewed.

7.1. WEATHERING MECHANISMS – CHARGED PARTICLES

Given the ubiquity of charged particles (ions) in the space radiation environment, much research attention has been paid to the potential contribution of three ion-bombardment-based space weathering mechanisms. The first of these is so-called "sputtering" of individual atoms from the surfaces of planetary bodies (Hapke, 2001), which are composed of generally porous materials (Noble et al., 2001). The physical process of sputtering in/from porous materials is highly complex, involving the bombardment of irregular surfaces (correlating to different angles of incidence), the angular and depth distribution of the ejected (sputtered) atoms and/or molecules as they relate to the molecular geometry of the material, and the re-deposition of atoms within and upon the internal and external surfaces of the material (Rodriguez-Nieva & Bringa, 2013). In the context of space weathering, it is believed that sputtering not only causes the atomic erosion or recession of a target surface (Kuhlman et al., 2015), but it is also responsible for the disassociation of iron from iron-bearing silicates and the subsequent deposition and accumulation of nanophase iron on material surfaces (Noble et al., 2007). However, it is worth noting that Brunetto and Strazzulla (2005) found sputtering to be physically

relevant only for ion flux densities greater than 1×10^{18} ions per cm^2 per second (cm^{-2} s^{-1}), whereas the slow and fast solar wind proton flux densities are only 3.7×10^8 cm^{-2} s^{-1} and 2.0×10^8 cm^{-2} s^{-1}, respectively (Balogh et al., 2001). This would seem to suggest that sputtering alone cannot be responsible for physical space weathering effects.

Secondly, the role of direct ion irradiation in solid materials is a process that has been a periodic focus of research, although it seems to a lesser degree than either the sputtering process described above or ion implantation as will be discussed below. In the present case, the progressive amorphization of a target's surficial micro-crystalline mineral structure has been found to occur due to the elastic collision of incoming ions and mineral nuclei, which results in both the darkening as well as the reddening of the UV-VIS-NIR spectral slope (Brunetto & Strazzulla, 2005). It is noteworthy that this was found to occur at lower particle flux densities than sputtering, e.g., $< 1 \times 10^{17}$ cm^{-2} s^{-1}. Their work demonstrated that solar wind irradiation, acting via the amorphization of the micro-crystalline structure of the uppermost layers of the target material, is a physical mechanism that acts in near-Earth space on a time-scale less than 10^6 years. This understanding is further enhanced by the practical work of Brunetto & Strazulla (2005), which finds that higher ionization energies correlate to more efficient albedo darkening and slope reddening.

The third solar-ion-bombardment process is that of ion implantation. In this case, solar protons (ionized solar hydrogen) in the 1 keV energy range can implant in the first 100 nanometers of surface material as hydrogen (Farrel et al., 2015). This, in turn, can function to reduce iron as part of the overall weathering process.

7.2. WEATHERING MECHANISMS – IONS VS. MICROMETEORITES

The proposition of a relationship between micrometeorite bombardment and the optical effects of space weathering reaches back nearly than a half-century (e.g., Hapke et al., 1975). At the time, the accumulation of dark, agglutinitic glass via micrometeorite impact melting of regolith was identified as an important contributor to the process of space weathering. However, the presence of the glass itself could not explain the spectral reddening associated with mature lunar soils (Kohout, et al., 2014). Since that time, it has been shown via pulse-laser laboratory simulations that the impacts of high-velocity, interplanetary dust particles result in the formation of nanophase iron and replicate the changes in optical properties observed on weathered bodies (Noble et al., 2011). Accordingly, these micrometeorite weathering effects are believed to be driven by the vaporization of surface materials and the formation of impact glasses incorporating nanophase iron particles (Sasaki & Kurahashi, 2004).

While solar wind was initially considered to be responsible for the production of weathering-linked nanophase iron via sputtering and ion implantation, research performed by Sasaki et al. (2001) demonstrated that the presence of hydrogen was unnecessary and that vapor deposition during micrometeorite impacts alone could be responsible for the production of nanophase iron. This cast into doubt which of the two space weathering processes (solar wind or micrometeorite impacts) were dominant or necessary. Consequently, the relative importance of ion bombardment versus micrometeoroid bombardment in producing nanophase iron is unclear to this day (Blewett et al., 2016).[6] However, it is worth noting that laboratory research has indicated that solar wind as a weathering mechanism is more efficient at spectral reddening and

[6] The salient inverse point may therefore be made that laboratory research appears to demonstrate that both meteorite and ion bombardment processes are capable of producing the entrained nanophase iron associated with space weathering.

darkening than vapor coating by micro-meteorite impacts (Brunetto & Strazzulla, 2005). Intriguingly, Brunetto et al. (2007) suggest based on laboratory results that micrometeoroid-bombardment-induced spectral reddening might be connected with a structural or morphological materials process, such as mineral amorphization.

While the typical micrometeorite environment in the plane of the Solar System is fairly well defined, commonly cited in dust impact research with values such as an impact rate for 1-μm interplanetary dust of approximately 10^{-4} m^{-2} s^{-1} and an impact velocity of roughly 20 km/s (e.g., Kissel & Kruger, 1987), the micrometeorite field at higher inclinations is more difficult to define. This current reality owes largely to the fact that so few spacecraft with adequate instrumentation have traveled to or through these higher-inclination environments. For these values, we must rely on information from the dust impactor instrumentation carried aboard the Ulysses spacecraft (Grun et al., 1992b), which revealed that generally, micrometeoroid mass and impact frequency decrease with increasing heliospheric latitude (Kruger et al., 2010). Section 2.2 provides additional discussion.

7.3. LUNAR SPACE WEATHERING

With a veritable sea of compositional and orbital variability in the population of airless bodies exposed to space weathering in the Solar System, one of the primary challenges is determining what space weathering information is "signal," and what is "noise." If one considers each weathered body in the Solar System as having the ability to reveal a portion of the weathering "puzzle," then a top-level overview of the current understanding of space weathering actions on bodies in the Solar System is warranted. In this light, it is sensible to begin with the most accessible example of space weathering, which is found on Earth's Moon.

Compared to the spectrum of freshly-powdered lunar rock, lunar soil that has undergone space weathering expresses reduced reflectance (i.e., lowered albedo), an increase in spectral slope (or spectral "reddening"), and muted mineralogical absorption bands (Blewett et al., 2016). Freshly exposed lunar material has been shown to gradually mature on the lunar surface until it reaches a steady-state of interrelating processes, referred to as the "equilibrium color." These optical changes have been related to the formation of impact glasses (Hemingway et al, 2015) and the accumulation of nanophase iron on and within regolith grains. This nanophase iron can be produced by the reduction of iron in silicates as well as by vapor deposition, potentially distinct processes caused either by micrometeoroid bombardment or solar-wind ion sputtering, or the production could result from a combination of solar wind hydrogen implantation "preparation" of a surface prior to a micrometeorite impact (Blewett et al., 2016).

However, and perhaps of critical importance to a more refined understanding of space weathering at large, are two recent lunar findings. The first discovery is that the equilibrium color of mature lunar soil, as well as 950 nm/750 nm band ratio, has been shown to vary predictably with lunar latitude; higher albedo trends toward the poles, and darker albedo trends toward the lunar equator. This links weathering effects to the flux of weathering contributors, those being either ion or micrometeoroid (Hemingway et al., 2015). The second discovery is that the magnetization of lunar crust has been strongly correlated with surficial albedo anomalies such as Reiner Gamma, located at the western side of the Oceanus Procellarum, which serves as a now-classic example of what is known as a "lunar swirl" (El-Baz, 1972). A computational validation of the magnetic nature of the swirls was performed most recently by Poppe et al. (2016), confirming that the swirls are magnetic in nature. Figure 9 presents an image of the

Reiner Gamma feature, which highlights the albedo features that correspond to the presence of remnant, local geomagnetic field lines.

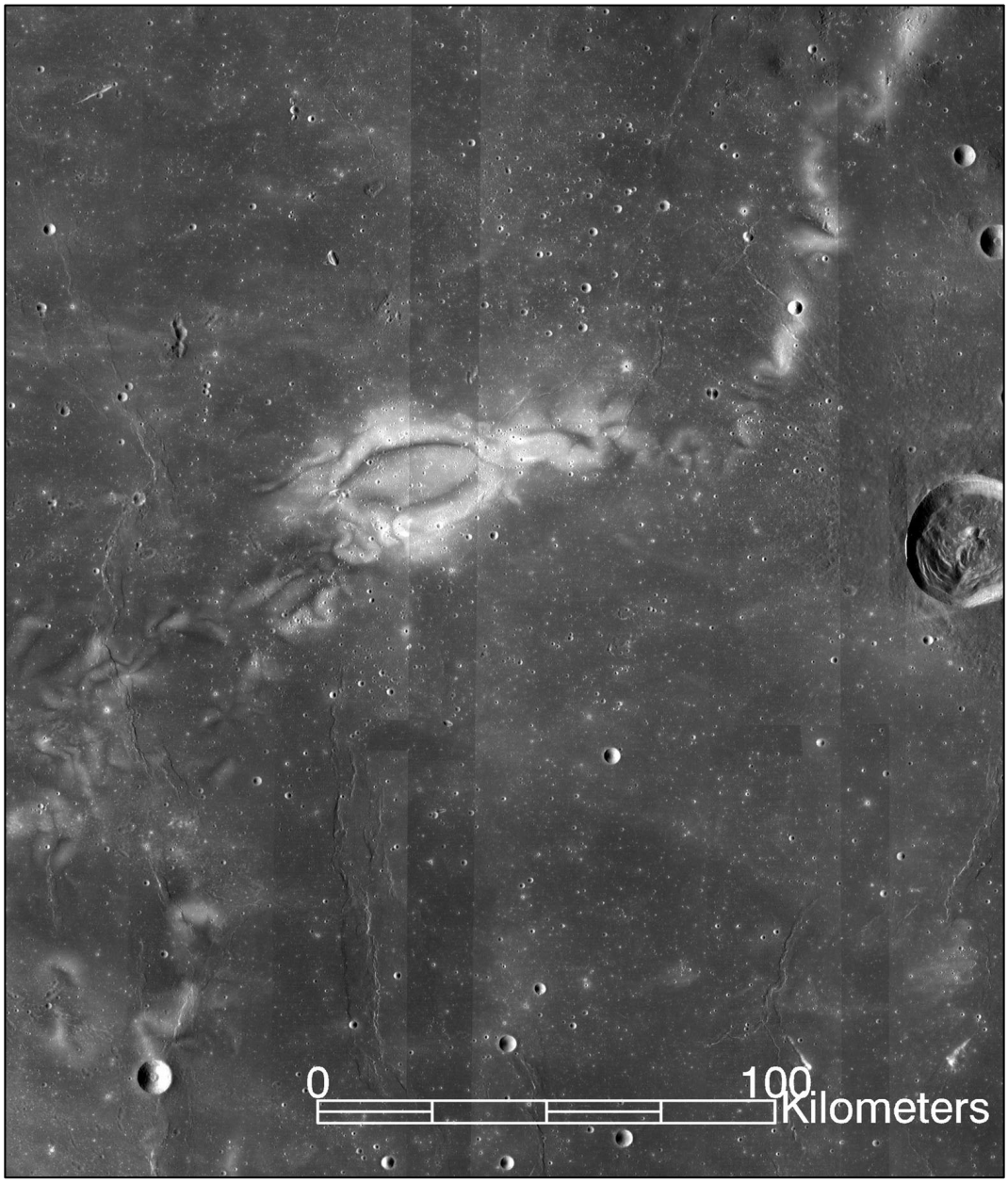

Figure 9. Image of the Renier Gamma lunar swirl

The Reiner Gamma lunar swirl as imaged by NASA's Lunar Reconnaissance Orbiter. Visible light and dark bands indicate the presence of remnant crustal magnetic fields, where light areas indicate less-weathered surfaces, and darker surfaces indicate more-weathered surfaces. (Image credit: NASA LRO WAC science team)

In fact, the implications of magnetically-correlated lunar swirls becomes a critical "Rosetta stone" for untangling the potential roles of solar ion bombardment versus micrometeoroid bombardment in lunar-style space weathering. To the point, Hemingway et al. (2015) consider that micrometeroid flux, like solar wind, varies with latitude due to decreasing angle of incidence. However, micrometeoroid flux would not be expected to vary significantly across the relatively discrete location of a lunar swirl. In contrast, solar wind flux would be reduced both with latitude as well as with lunar swirls, where strong geomagnetic fields act to shield the lunar surface from charged-particle bombardment. Therefore, after finding statistical equivalence in the observed lunar latitudinal color variation and the color variations expressed in lunar swirls, the researchers were able to conclude that solar wind flux, and not micrometeoroid flux, must be a dominant contributor to at least the albedo-darkening aspect of the space weathering process in the lunar case, and micrometeoroid flux was thereby eliminated as the driving lunar space weathering mechanism.

Further, Hemingway et al. (2015) evolve their suggested model to match observations by proposing that a solar-wind-flux-dependent form of weathering is rapid, reaching equilibrium on timescales of 10^5 to 10^6 years, with an albedo maturation effectiveness approximately 3.6 times that of micrometeorite impacts but with only a small effectiveness in altering mineralogical absorption features. Micrometeroite impacts, on the other hand, are suggested to possess greater effectiveness in altering absorption features and are implied to operate on much longer timescales, working to bring terrain of varying states of maturation to a broader temporo-spatio color equilibrium driven by the micrometeorite flux and physical regolith mixing, sorting, and fining processes.

As it has been previously established, because ion bombardment will act to significantly weaken the structural properties of a material (Brunetto & Strazzulla, 2005; Djurabekova et al., 2012; Zinkle, 2012), it is tempting to integrate the two processes by proposing that ion bombardment functions as an essential precursor for classical, lunar-style space weathering, which is herein proposed as a hybrid style of weathering that includes both ion bombardment and micrometeorite impacts (Poppe et al., 2016). By extension, under a condition of reduced ion flux, a slower rate of micrometeorite-only weathering is implied, which is more efficient at altering mineral absorption features but is less effective at maturing surficial albedo.

7.4 SPACE WEATHERING ON MERCURY

Mercury also appears to undergo lunar-style space weathering, where fresher material correlates to higher reflectance (higher albedo) and is less red than mature Mercurian soils (Blewett et al., 2016). Because Mercury is known to possess a global magnetic field, it can be argued that if ion bombardment were a dominant contributor to space weathering processes (as has been recently suggested in the lunar case), one would also expect the degree of magnetic protection to vary with latitude toward the magnetic poles and weathering rates to correlate with it (Sarantos et al., 2007). Because no such albedo-latitude relationship has yet been identified, untangling the driving mechanisms behind lunar-style weathering has been frustrated in the first order by the Mercury example.

However, by assessing relevant differences between Mercury and the Moon, potential explanations for the discrepancies in style between lunar and Mercurian space weathering can be unearthed. The first of these pertinent differences include the fact that the dust flux on the Mercury surface is approximately ten times higher than the rate of infalling dust found at the lunar surface. Secondly, due to both orbital parameters of orbiting dust and the larger mass of the

planet itself, micrometeoroid impact velocity is nearly twice that experienced on the lunar surface (Sasaki & Kurahashi, 2004). Together, this results in approximately 14 times more impact melt and 20 times the production of impact vapor on the Mercurian surface than on the lunar surface (Blewett et al., 2010).

Consequently, in the Mercury case, while weathering is lunar-styled in terms of expression, it is entirely possible that the rate of space weathering by micrometeorite bombardment overwhelms the effects of ion bombardment, tipping the scales in favor of micrometeorite bombardment as the dominant weathering process on Mercury. Given the findings of Hemingway et al. (2015), this would suggest the existence of a boundary condition as one moves toward the inner Solar System where the dominance of solar wind as a primary weathering mechanism gives way to that of micrometeorite bombardment due to overall greater impact energies. Secondarily, this suggests that an overall mass limit exists beyond which the energy of micrometeorite bombardment can overwhelm other mechanisms (see the discussion of trending in albedo and object size in the following section).

7.5 DIVERSE SPACE WEATHERING ON S-TYPE ASTEROIDS

Perhaps the most intriguing portion of the space weathering phenomenon concerns the apparently contradictory nature of weathering observed on S-type asteroids (Gaffey, 2010). While one might expect lunar-style space weathering to occur on Near-Earth Asteroids (NEAs) as well as Main Belt objects due to their similar compositions and exposure rates, the reality is much less straightforward and implies at least three separate styles of weathering (albedo-darkening without spectral modification, spectral modification without albedo-darkening, and those that express both albedo-darkening and spectral modification, i.e., lunar-style space

weathering). Figure 10 presents a schematic diagram of these styles, which is adapted from Gaffey (2010).

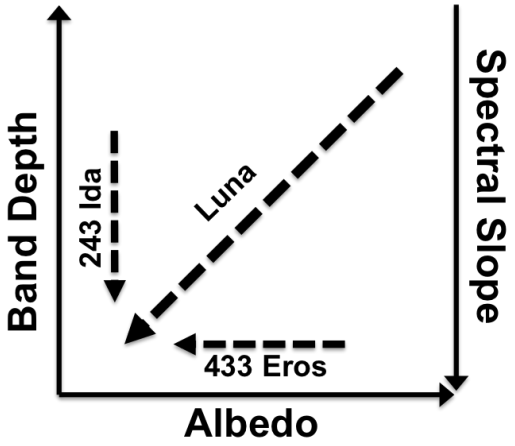

Figure 10. Schematic diagram of space weathering spectral-albedo correlations

Combined schematic representation of space weathering spectral–albedo correlations for the key examples of the Moon (Luna) and S-type asteroids 243 Ida and 433 Eros. Axis arrows indicate the direction of increasing value, and plotted arrows indicate the apparent effect of increased weathering on each body (Adapted from Gaffey, 2010).

Indeed, complicating factors include the reality Thomas et al. (2011) and Trilling et al. (2010) report a persistent positive trend in the overall albedo of S-complex (and Q-complex) objects with decreasing object diameter. However, due to the relative novelty of orbiting or fly-by opportunities to obtain detailed measurements of S-type asteroid surfaces, there are only four key examples of well-studied S-complex (or related) asteroids in terms of their varied forms of space weathering. These are briefly reviewed in the subsections to follow.

7.5.1 – 243 IDA

A Main Belt object nearly 31 km in diameter, 243 Ida expresses a departure from lunar-style space weathering, where spectral reddening and absorption-weakening were observed, but its albedo, at a value of 0.262, has remained relatively unaltered (Gaffey, 2010; Blewett et al.,

2016). The work of Hemingway et al. (2015) suggests that strong absorption modification features without strong albedo effects would implicate micrometeorite impacts as a driving weathering mechanism. With an orbital inclination of only 1.1 degrees, 243 Ida would not be expected to experience any enhanced fast solar wind exposure when compared to the nominal radiation exposure in the Solar System invariant plane.

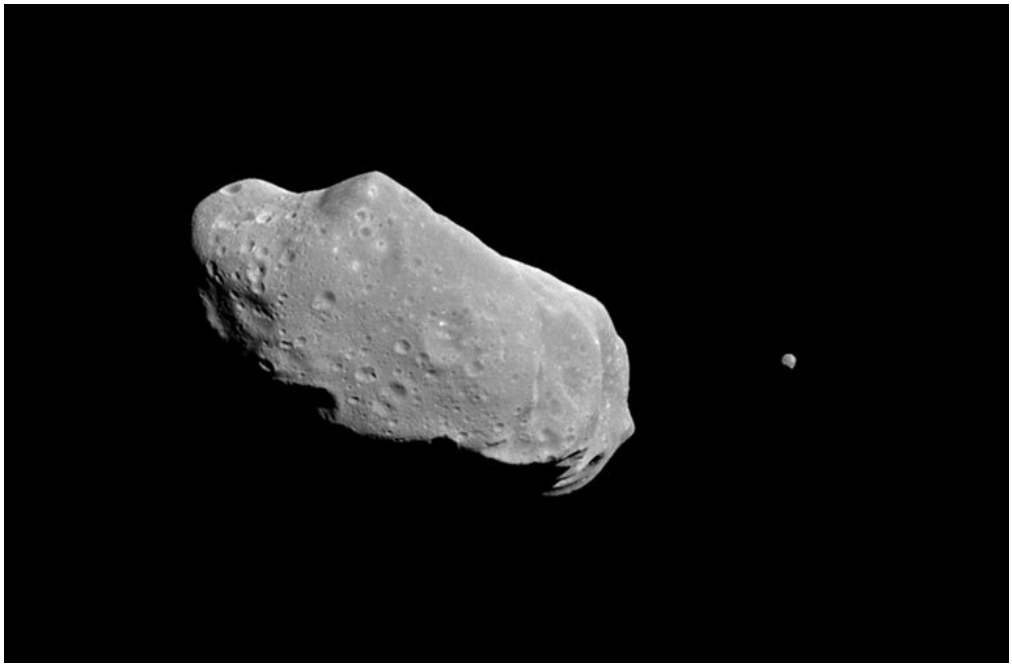

Figure 11. Asteroid 243 Ida

Asteroid 243 Ida and moon Dactyl as imaged by the Galileo spacecraft in 1994. (Image credit: NASA/JPL)

7.5.2 – 433 EROS

A ~33 km-long Near Earth Asteroid (NEA), 433 Eros clearly expresses a lunar-style albedo relationship, where more mature soils are darker and an overall albedo of 0.25. However, these reflectance characteristics do not correlate with the expected spectral reddening or absorption band weakening (Gaffey, 2010; Blewett et al., 2016). The work of Hemingway et al. (2015) suggests that strong albedo effects without modified color or absorption features implicate solar wind as a driving weathering mechanism. With an orbital inclination of 10.8

degrees, 433 Eros would be expected to experience enhanced fast solar wind exposure, located between 15 and 18 degrees heliographic latitude, when compared to the nominal radiation exposure in the Solar System invariant plane.

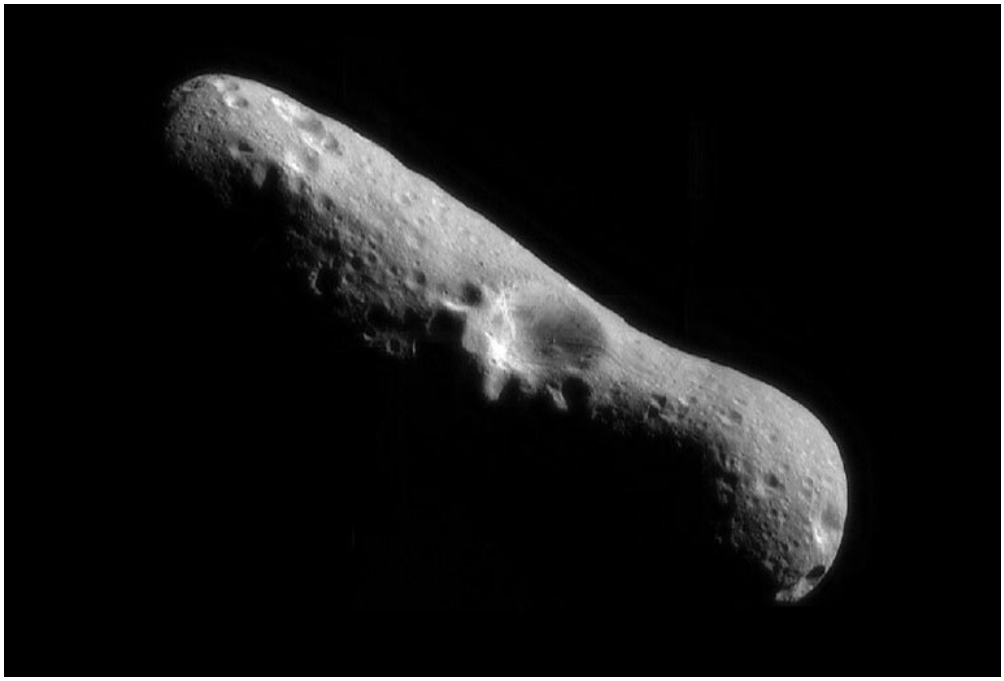

Figure 12. Asteroid 433 Eros

Asteroid 433 Eros as imaged by the NEAR Shoemaker spacecraft in 2000. (Image credit: NASA/JPL)

7.5.3 – 951 GASPRA

A ~12 km diameter S-type asteroid located in the Main Belt, 951 Gaspra is notable in that it obeys lunar-style space weathering. Specifically, surface darkening (overall albedo of 0.246) correlates with spectral reddening and weaker absorption bands (Gaffey, 2010; Blewett et al., 2016). The work of Hemingway et al. (2015) suggests that true lunar-style weathering represents an equilibrium state between shorter and longer-period weathering rates related to ion and micrometeoroid flux rates. With an orbital inclination of 4.1 degrees, 951 Gaspra would not be expected to experience any enhanced fast solar wind exposure when compared to the nominal radiation exposure in the Solar System invariant plane. However, it may be noteworthy that its

orbit carries it closer at maximum (11.35 degrees) to the 15-degree fast-wind transition zone than objects more squarely within the Solar System invariant plane.

***Figure 13.** Asteroid 951 Gaspra*

Asteroid 951 Gaspra as imaged by the Galileo spacecraft in 1991. (Image credit: NASA/JPL)

7.5.4 – 25143 ITOKAWA

Similar in space weathering expression to 243 Ida, 25143 Itokawa is a NEA that evidences spectral reddening associated with band weakening but without a strong albedo relationship (Blewett et al., 2016). 25143 Itokawa possesses a wide range of surface reflectivity, with albedo values ranging from 0.23-0.53. The work of Hemingway et al. (2015) suggests that strong absorption modification features without strong albedo effects would implicate micrometeorite impacts as a driving weathering mechanism. This is bolstered by the return of sample grains from Itokawa that showed the presence of variable mictization (compared to the thicker amorphous silicate layers observed on lunar grains), evidence of vapor deposition, along

with smaller nanophase iron particles (<10 um), which appear to efficiently redden spectra without darkening it (Noguchi et al., 2011). Like 243 Ida, with an orbital inclination of only 1.65 degrees, 25143 Itokawa would not be expected to experience any enhanced fast solar wind exposure when compared to the nominal radiation exposure in the Solar System invariant plane.

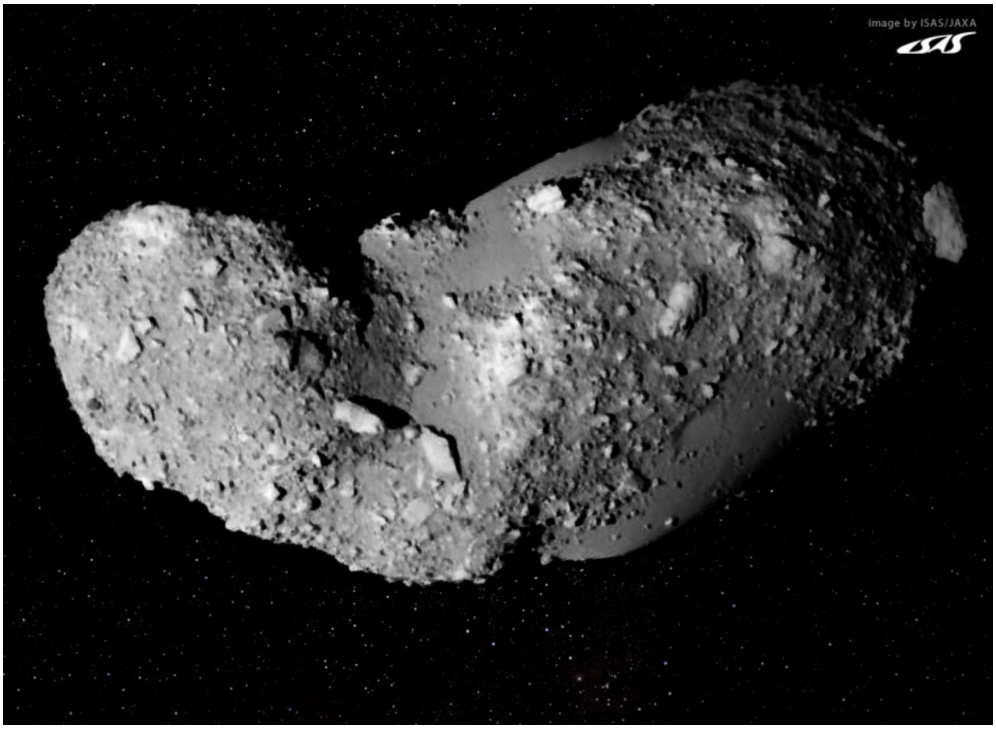

Figure 14. Asteroid 25143 Itokawa

Asteroid 25143 Itokawa as imaged by the Hayabusa spacecraft in 2005. (Image credit: JAXA/ISAS)

7.6 ANTI-WEATHERING "FRESHENING" PROCESSES

Lastly, recent propositions have speculated that space weathering mechanisms may be further obfuscated by working against so-called "freshening" mechanisms, such as the fly-by and gravity perturbation mechanism proposed by Binzel et al. (2010) and further evolved by DeMeo et al. (2014). This concept describes a means for gravitational interactions with larger bodies to perturb and disrupt the orientation of weathered surface grains, effectively resetting the apparent weathering condition of the surface (akin to kicking over a rock covered with patina in the

Mojave Desert). While the existence of such a mechanism is currently debated, this process is believed to operate more strongly on airless bodies that travel furthest inward into the Solar System, thereby maximizing the potential opportunities for gravitational interactions with the inner planets. By extension, this may prove relevant as an additional source of space weathering heterogeneity among airless bodies, and this "planetary-encounter theory" will be revisited in the analysis section to follow.

7.7 "HEMINGWAY MATRIX" OF S-TYPE WEATHERING

Using the Renier Gamma magnetic deflection-albedo relationship revelation as a guide, the Hemingway et al. (2015) research suggests a tantalizing link between space weathering driven by solar ion bombardment to instances of more pronounced albedo-darkening and reddening effects without associated spectral modifications.[7] By extension, the work would therefore also link more pronounced modification of spectral absorption features without a correlating drop in reflectance to space weathering dominated instead by micrometeorite impacts. Lunar-style space weathering, then, would represent a sort of equilibrium state where both mechanisms act as contributors to the overall maturation of target surfaces.

With this in mind, Table 3 presents what is almost certainly an over-simplified matrix, referred to here as a "Hemingway Matrix," of the hypothetical dominant weathering mechanism/style and physical/orbital characteristics for each of the four S-complex asteroids referenced in the previous sections, which can provide useful context for the analysis to follow.

[7] It is noteworthy that this suggestion agrees with the laboratory work of Brunetto & Strazzulla (2005).

Table 3 – Space-weathering style and asteroid orbital attribute matrix

Asteroid Name	Orbit Type	Dominant Weathering Style*	Diameter (km)	Inclination (degrees)	Max Heliographic Latitude** (degrees)
243 Ida	Main Belt	Micrometeoroid	~31	1.1	18.35
433 Eros	NEA	Ion Bombardment	~33	10.8	28.05
951 Gaspra	Main Belt	Lunar	~12	4.1	21.35
25143 Itokawa	NEA	Micrometeoroid	~0.6	1.6	18.85

* Inspired by the work of Hemingway et al. (2015), which signals albedo-darkening space weathering as being ion-bombardment dominant, spectral-modification space weathering as being micrometeorite-dominant, and lunar-style weathering as a combination of the two.

** Max Heliographic Latitude differs from a simple inclination-to-latitude conversion and conveys the maximum potential latitude at which a body could spend a significant fraction of its orbit when including the potentially-coincident effect of solar axial tilt (approx. 7.25 degrees) as well as the tilt of the solar dipole with respect to the solar axis (approx. 10 degrees).

As is evident in Table 3, neither the size nor orbit type of a given asteroid correlate with the object's corresponding hypothesized space weathering style in a straightforward way. However, a general correlation to weathering style does exist with respect to an asteroid's maximum heliographic latitude. Following the scheme suggested by the Hemingway (2015) research, both styles of space weathering that express albedo-darkening, being lunar-style space weathering and ion-bombardment-dominant space weathering, rely on a significant contribution of ion bombardment. Given that solar wind (ion) energy increases with heliographic latitude (see Section 2.3), it would follow that these styles would correlate with those bodies that have the steepest maximum heliographic latitude, and ideally, would extend past the transition zone at ±15-25 degrees latitude into the consistently-fast solar wind. Table 3 demonstrates this reality: 951 Gaspra and 433 Eros, the objects with the highest orbital inclinations, are the two airless bodies that experience solar-wind dominated or lunar-style space weathering; the maximum heliographic latitude reached by each extends well beyond the transition latitude of ±15 degrees to either near or beyond the clear fast-wind boundary at ±25 degrees, with the steepest inclination of the two experiencing ion-bombardment-dominated weathering. In contrast, both

243 Ida and 25143 Itokawa, with inclinations <2 degrees (within the ecliptic), do not approach or clearly breach the fast-wind latitudes beyond ±25 degrees, and they each experience micrometeorite-dominated space weathering. It is also noteworthy that 433 Eros and 25143 Itokawa, both NEAs, might otherwise be expected to conceptually experience the same style of space weathering. However, the parameter of orbital inclination and resulting maximum heliographic latitude serve to clearly divide these two similar bodies into two very different ion bombardment regimes, conceptually supporting the present investigation.

8.0 RESULTS AND DISCUSSION

The performance of a series of statistical analyses of the dataset as described in Sections 5.0 and 6.0, as well as an overview of the consequent findings, is described in the subsections to follow.

8.1 TOTAL S-TYPE STUDY POPULATION

A plot of the relationship of albedo (Spitzer-based) to orbital inclination in the target population (SMASS-based) is presented in Figure 15, below. Note that this includes the entire study population of 71 bodies, which includes all S-type and subtype asteroids in the SMASS-II

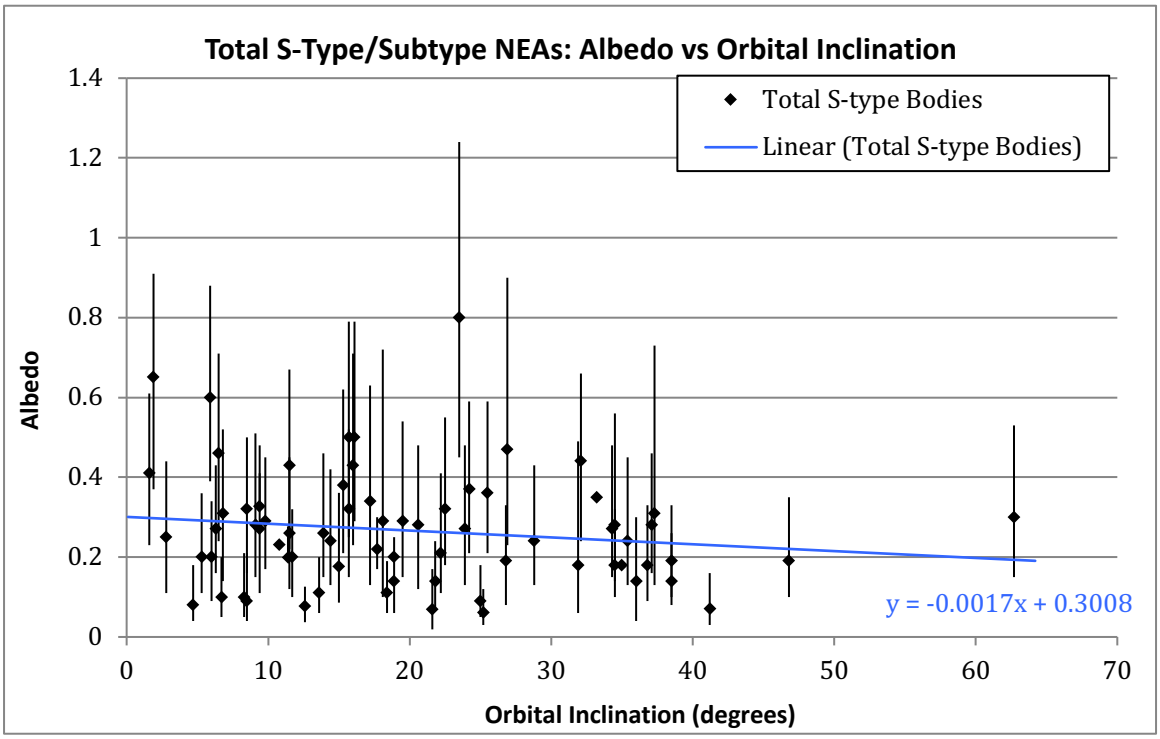

Figure 15. Albedo vs orbital inclination for the total S-type study population

Plot of all available Spitzer telescope-derived albedos for the gross population of SMASS-II S-type and S-subtype asteroids. Vertical bars represent albedo error (see Table 1).

survey for which there was available Spitzer telescope albedo information, contributing what is likely a non-trivial degree of compositional variation to the overall study population.

Without accounting for potential associated complicating factors, such as compositional details of asteroid subtype or orbital parameters other than inclination, a simple linear regression demonstrates a small but persistent negative correlation between albedo and inclination. With an *r*-value for the population of -0.1495, the absolute value of which exceeds the critical value of 0.1380 at the 75% confidence level, the null hypothesis that there is no correlation between albedo and inclination can be rejected, and the negative relationship between orbital inclination and albedo is thereby shown to be statistically significant. Indeed, with a regression slope of -0.17% albedo per degree increase in orbital inclination, this trend agrees with what would be expected if increased exposure to fast solar wind did serve as a driver for the albedo-darkening mechanism of space weathering. However, in order to determine if the presence of S-complex subtypes further reinforce or oppose an apparent albedo-inclination relationship, it is necessary to evaluate each subtype independently.

8.2 CORE S-TYPE POPULATION

An assessment performed in parallel to the analysis discussed in Section 8.1 but without any of the S-complex subtypes included is reported in this section. Perhaps most noteworthy is that a linear regression of the S-type "core" asteroids within the study population reveals precisely the same trend as that observed in the total population reported in the previous section (-0.17% albedo per degree increase in inclination), though in this instance with a slightly elevated intercept. This may be interpreted as a slightly higher average unweathered albedo for the S-types than the total S-complex average, which will also be considered in the subsections to follow. This regression analysis for the restricted S-types is presented in Figure 16.

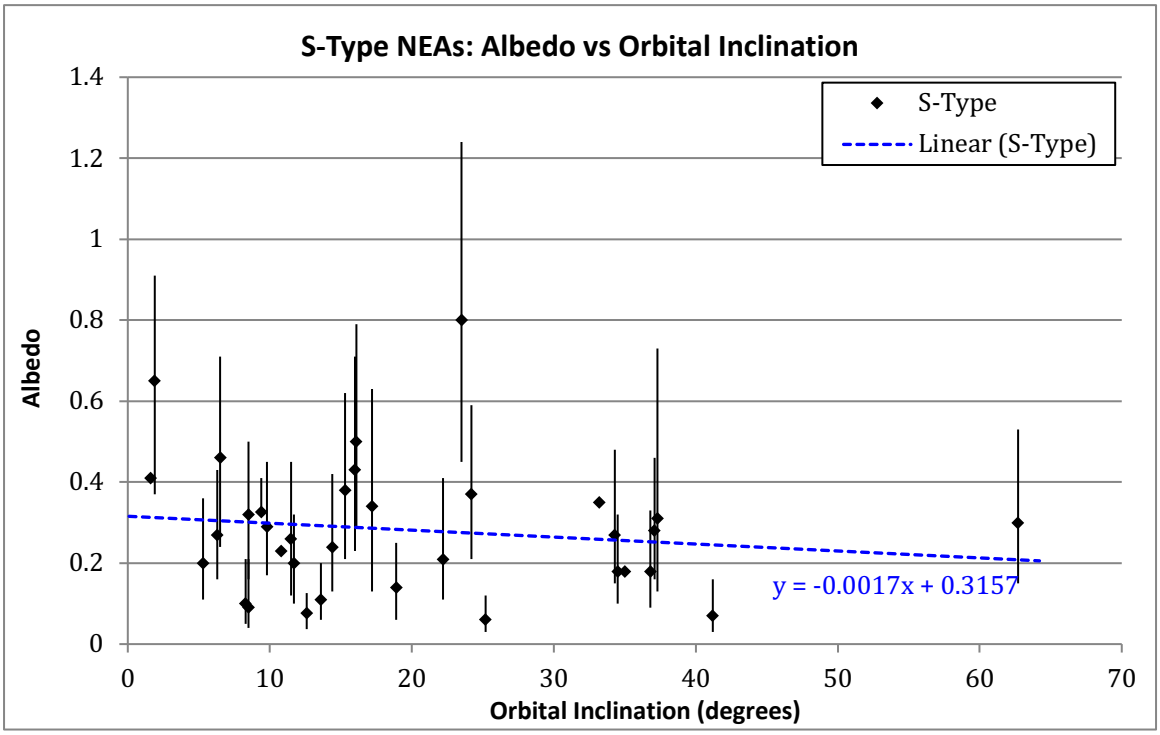

Figure 16. Albedo vs orbital inclination for the restricted S-type study population

Plot of Spitzer-telescope-derived albedos for the restricted population of SMASS-II S-type asteroids, from which all transitional subtypes have been removed. Vertical bars represent albedo error (see Table 1).

However, given a calculated correlation coefficient *r*-value for this analysis of -0.1466 and a dramatically-reduced sample population of 34 bodies, the absolute value of *r* determined in this instance does not exceed the critical value of 0.2028 at the 75% confidence interval. Consequently, this relationship cannot be shown to be statistically significant. In other words, it cannot be ruled out that the observed variability in the data is not simply due to intrinsic statistical sampling error under a condition where the null hypothesis is true, and there is not correlation between albedo and inclination for this population of asteroids. It is worth noting that the broad mineralogy of the primary S-type asteroids may be responsibility for a wide variability in weathering expression, which in combination with a small sample size could act to reduce the statistical significance of the same trending seen in Section 8.1.

8.3 Sk-SUBTYPE POPULATION

An assessment performed in parallel to the analysis discussed in Section 8.1 on only the Sk-subtype asteroids is reported in this section. Despite an extremely small sampling, this group expresses the steepest potential correlation between albedo and inclination and also the most tightly clustered. This Sk-subtype regression analysis is presented in Figure 17.

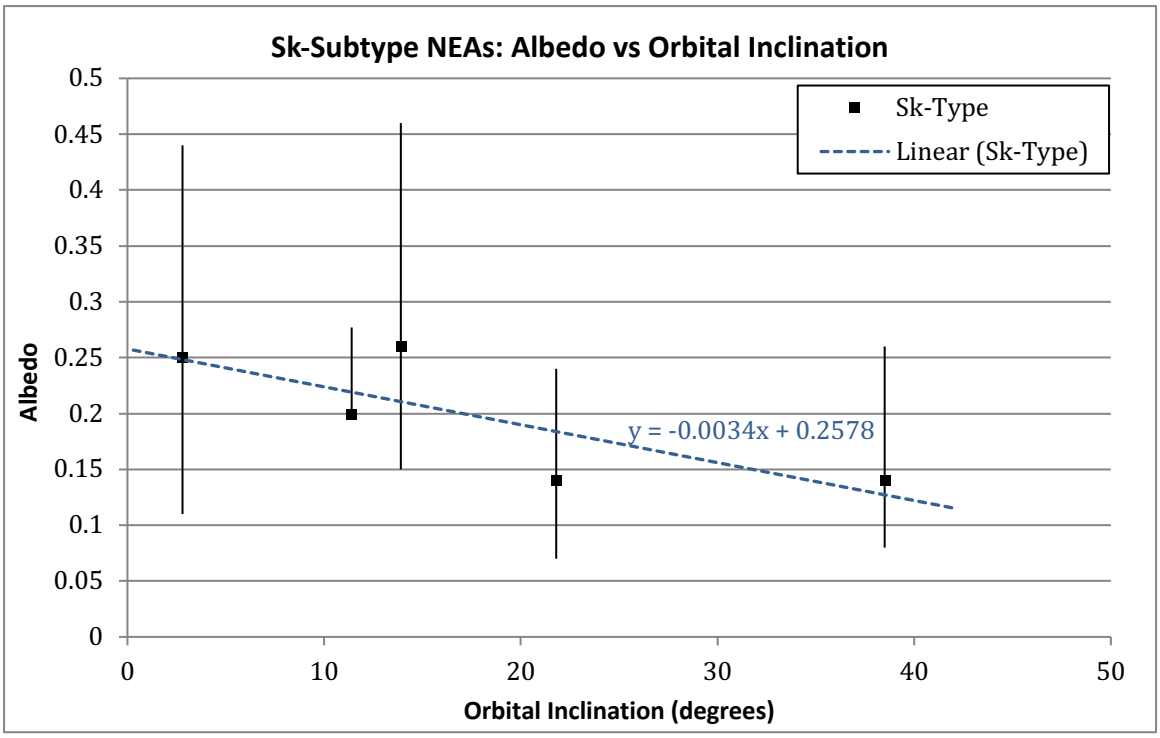

Figure 17. Albedo vs orbital inclination for the restricted Sk-subtype study population

Plot of Spitzer-telescope-derived albedos for the restricted population of SMASS-II Sk-subtype asteroids. Vertical bars represent albedo error (see Table 1).

The linear regression demonstrates a persistent negative correlation between albedo and inclination. With a calculated correlation coefficient *r*-value for the population of -0.7929, the absolute value of which exceeds the critical value of 0.6347 at the 75% confidence level, the null hypothesis that there is no correlation between albedo and inclination can be rejected in this case despite such a small sample group, and the negative relationship between orbital inclination and

albedo is thereby shown to be statistically significant. Indeed, with a regression slope of -0.34% albedo per degree increase in orbital inclination, exactly twice that of the total population as well as that of the generic S-types, this trend agrees with what would be expected if increased exposure to fast solar wind did serve as a driver for the albedo-darkening mechanism of space weathering. Given that the K-type asteroids, to which the Sk-subtype is understood to be transitional, are known to possess the lowest-albedo of any of the proximal classes to the S-type, these results may be in some senses surprising, as it could be reasonably assumed that albedo effects might be most difficult to distinguish in this case, making the statistical significance of an inclination-albedo correlation all the more noteworthy.

8.4 Sl-SUBTYPE POPULATION

An assessment performed in parallel to the analysis discussed in Section 8.1 on only the Sl-subtype asteroids is reported in this section. Representing the smallest sampling of the study (four samples), this subtype was seen to express a slightly-steeper inclination-albedo relationship than the average (-0.23% albedo per degree increase in inclination). This regression analysis for the Sl-subtype is presented in Figure 18.

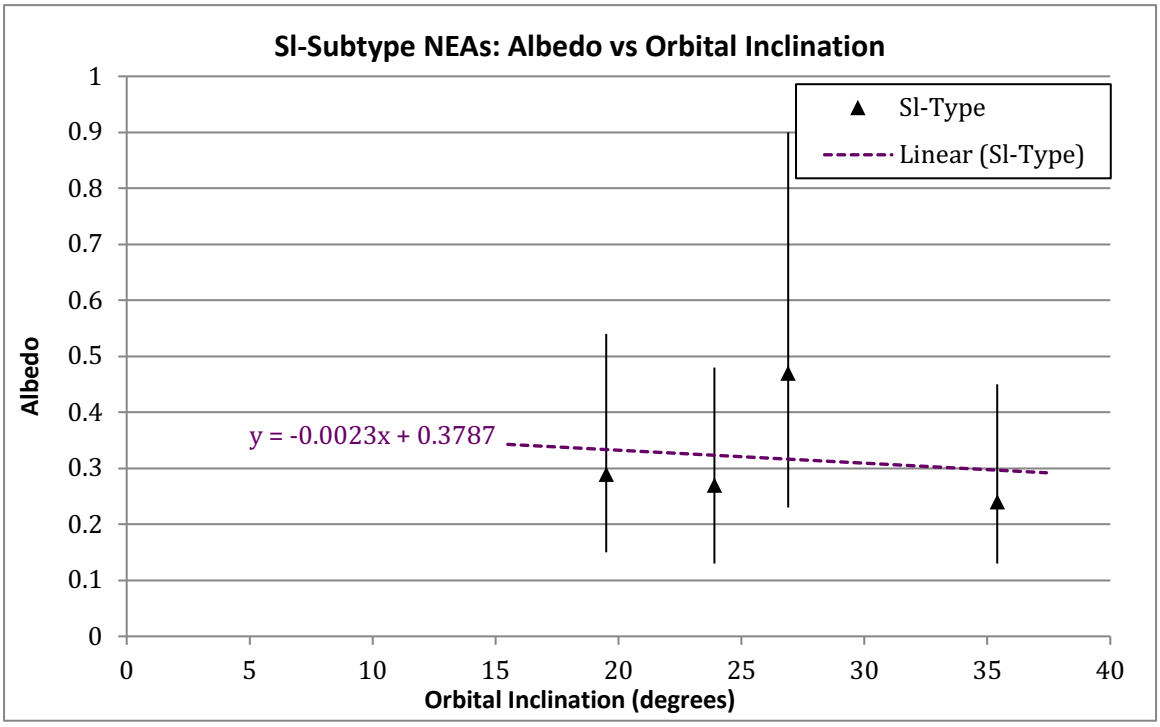

***Figure 18.** Albedo vs orbital inclination for the restricted Sl-subtype study population*

Plot of Spitzer-telescope-derived albedos for the restricted population of SMASS-II Sl-subtype asteroids. Vertical bars represent albedo error (see Table 1).

However, given a calculated correlation coefficient *r*-value for this analysis of -0.1498 and a sample population of only 4 bodies, it is perhaps unsurprising that the absolute value of *r* determined in this instance does not exceed or even approach the critical value of 0.7500 at the 75% confidence interval, and so this relationship cannot be shown to be statistically significant.

8.5 Sq-SUBTYPE POPULATION

An assessment performed in parallel to the analysis discussed in Section 8.1 on only the Sq-subtype asteroids is reported in this section. With the second-largest sampling in the study but one of the widest spread of constituent albedos, this sample group ultimately expressed a shallower potential correlation between albedo and inclination than the core S-types (-0.11%

albedo per degree increase in inclination). This Sq-subtype regression analysis is presented in Figure 19.

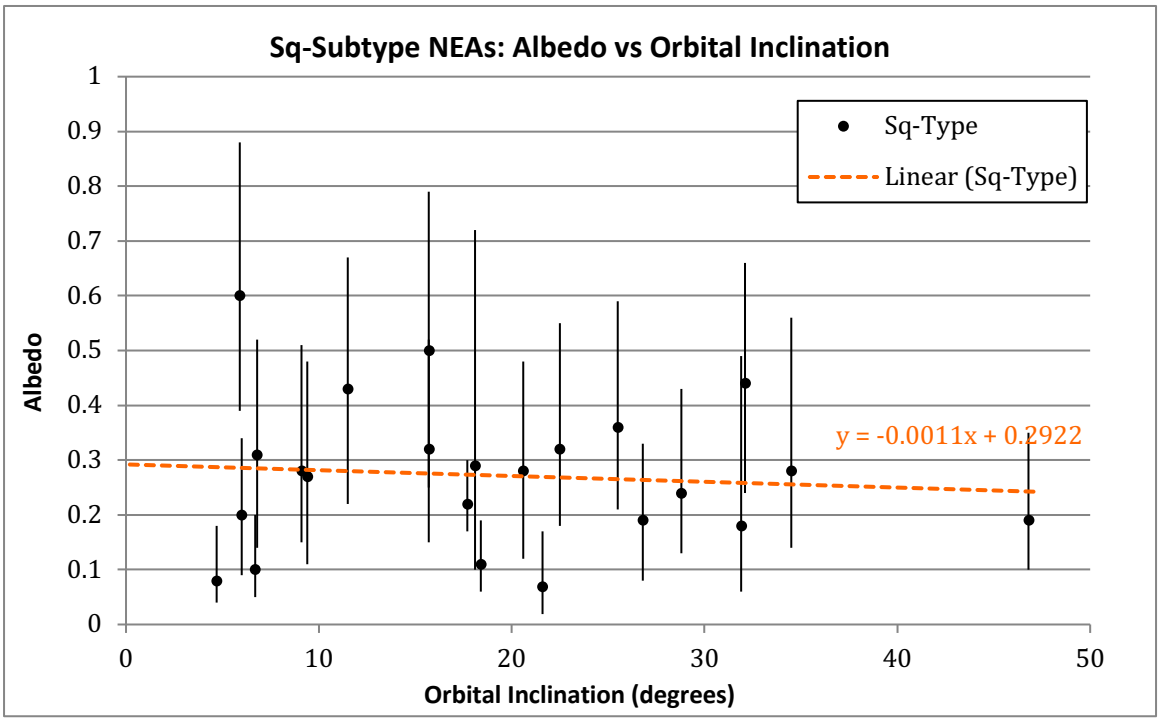

***Figure 19.** Albedo vs orbital inclination for the restricted Sq-subtype study population*

Plot of Spitzer-telescope-derived albedos for the restricted population of SMASS-II Sq-subtype asteroids. Vertical bars represent albedo error (see Table 1).

With a calculated correlation coefficient *r*-value of -0.0875, the absolute value of *r* determined in this instance does not exceed the critical value of 0.2500 at the 75% confidence interval, and so this relationship cannot be shown to be statistically significant. However, if there is any truth to the proposition that some S-type asteroids represent weathered Q-type bodies, then it is worth considering that a wide distribution of potential albedos in the transitional Sq-subtype would be expected, as they may represent fragments of Q-type bodies under varies stages of space weathering maturation.

8.6 Sr-SUBTYPE POPULATION

An assessment performed in parallel to the analysis discussed in Section 8.1 on only the Sr-subtype asteroids is reported in this section. With an extremely small sampling of only five bodies, this group expresses the shallowest potential correlation between albedo and inclination of all of the assessed subtypes in the study population. This Sr-subtype regression analysis is presented in Figure 20.

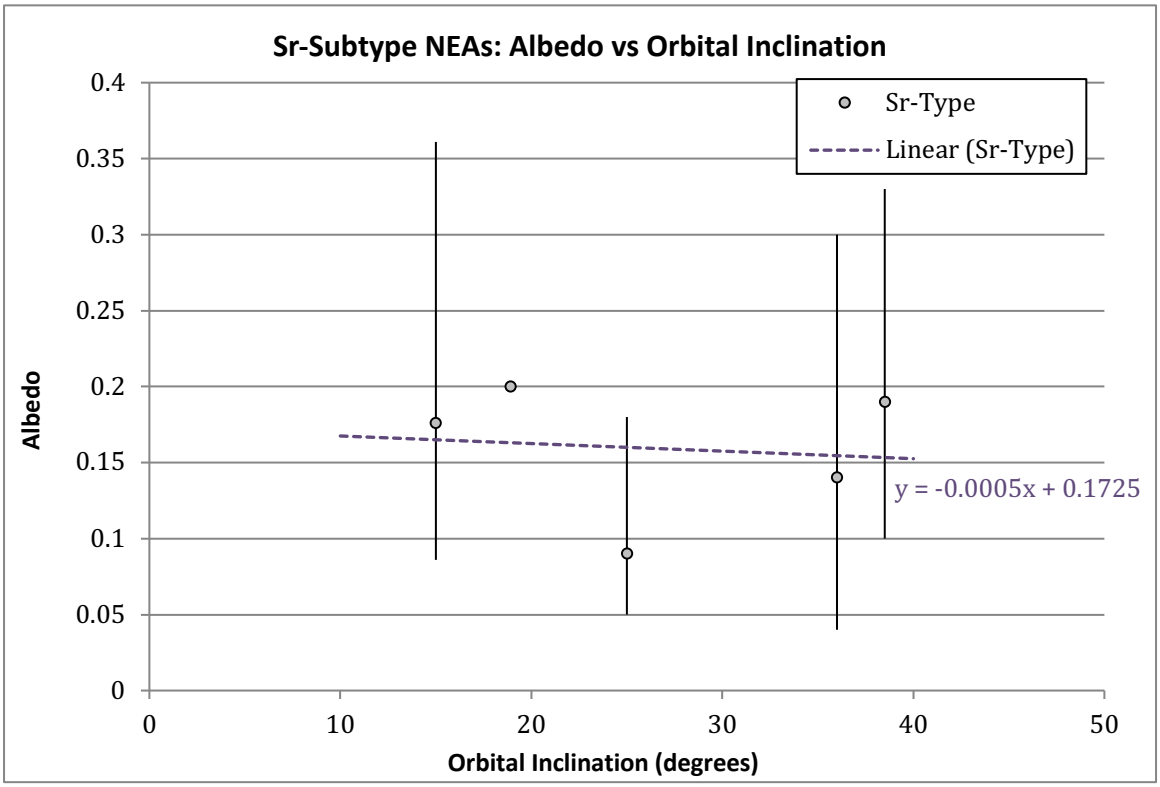

Figure 20. Albedo vs orbital inclination for the restricted Sr-subtype study population

Plot of Spitzer-telescope-derived albedos for the restricted population of SMASS-II Sr-subtype asteroids. Vertical bars represent albedo error (see Table 1).

With a calculated correlation coefficient *r*-value for this analysis of -0.0595 and a limited sample population of 5 bodies, the absolute value of *r* determined in this instance does not

exceed the critical value of 0.6347 at the 75% confidence interval. Consequently, this relationship cannot be shown to be statistically significant.

8.7 ANALYSIS OF REGRESSION COVARIANCE BY SUBTYPE

While not each of the S-subtypes indicated a significant inclination-albedo trend at the given population size, an analysis of covariance was performed between the regression lines for each population group in the study (excluding the total population regression, which would duplicate all values and artificially inflate the population agreement). These are presented in Figure 21.

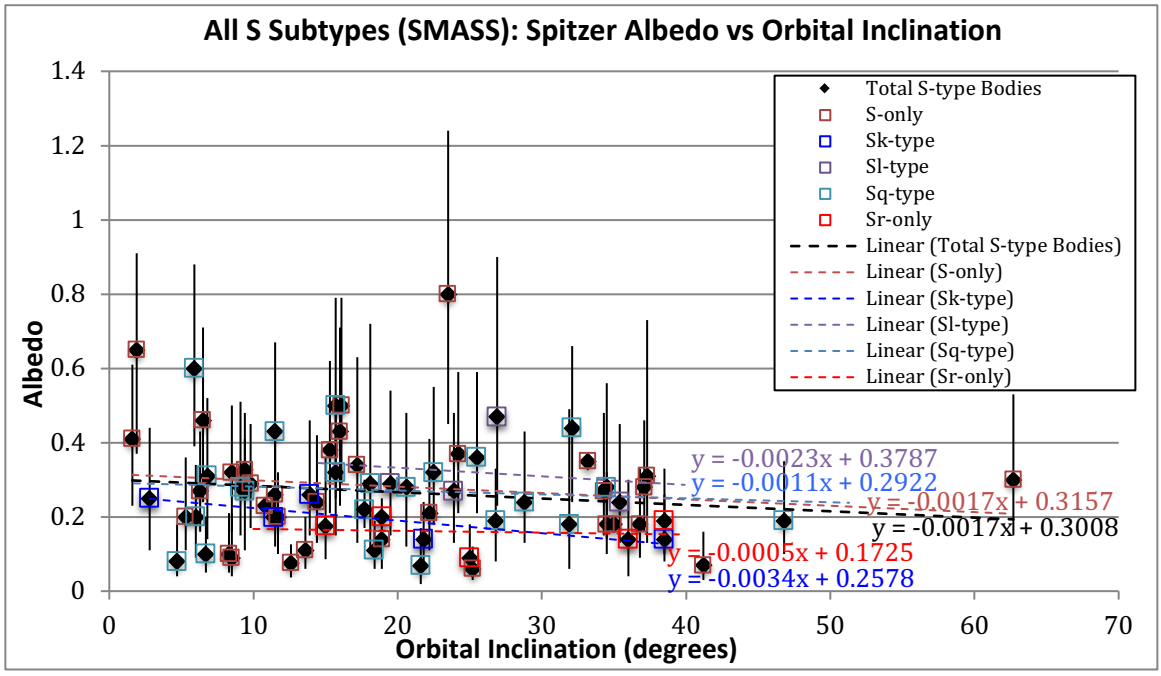

Figure 21. Combined plot of albedo vs orbital inclination for all S-complex subtypes

Plot of albedo-inclination regression lines for the population of S-type and S-subtype asteroids under study. Vertical bars represent albedo error (see Table 1).

Recall that the null hypothesis for an analysis of covariance between regression lines is that there is no difference between the slopes of the respective regressions. Additionally, recall

that the level of significance (*a*) for the present study was selected at 0.25. Being that statistical significance can be determined by the production of a P value less than the value of *a* (Natrella, 2005), the analysis of covariance between the regression lines failed to disprove the null hypothesis to an extremely high confidence level, expressing a P value of 0.99552 (where a value < 0.25 would have been required to disprove the null hypothesis to the 75% confidence level). In other words, the slopes of the regression lines were found to agree to an extremely high degree of significance, a finding which suggests one of two options: 1) that those S-subtype trends between albedo and inclination that were not found to be statistically significant (see Sections 8.2 and 8.4-8.6) were also real but failed the significance test due to a lack of statistical robustness resulting from low sample size, or 2) that an as-yet-identified bias exists in the Spitzer observational/data collection process or processing methodology, which falsely lowers the albedos of objects with increasing inclination. Additional investigation is necessary in order to determine which of these options is more likely.

8.8 CONSIDERING ORBITAL PARAMETERS

When considering the global suggestion of a relationship between orbital inclination and albedo-darkening due to ion-bombardment-based weathering effects in the context of the analysis performed in Section 8.6, it is fruitful to innovate alternative means to disprove the hypothesis. With this in mind, an effort to conceptualize inclination-albedo effects against the potential effects of "freshening" mechanisms was undertaken (see Section 7.6). From this perspective, presuming for the moment that the statistically-significant (to the 75% confidence level) findings of the previous section hold true, one would expect a secondary pattern to be preserved within the dataset when combined with the driving parameter behind surface freshening, which is the probability of planetary interactions. As the likelihood of the

interactions goes up with orbit crossings, the NEA orbits types that would be expected to subject an airless body to a probability of surface freshening encounters, in order of least to most, are Amor (farthest from the Sun and not Earth-crossing), Apollo (farther from the Sun but Earth-crossing), and Aten (closer to the sun and Earth-crossing). Consequently, if the population of NEAs under study were reassessed in terms of orbit type rather than S-subtype, one would still expect all populations to express a negative albedo-inclination slope, but the Amor population would be predicted to possess the shallowest slope, the Apollo subset would be predicted to possess the intermediate slope, and the Aten subgroup would be predicted to have the steepest inclination-albedo slope. This regression analysis was performed and is presented as Figure 22.

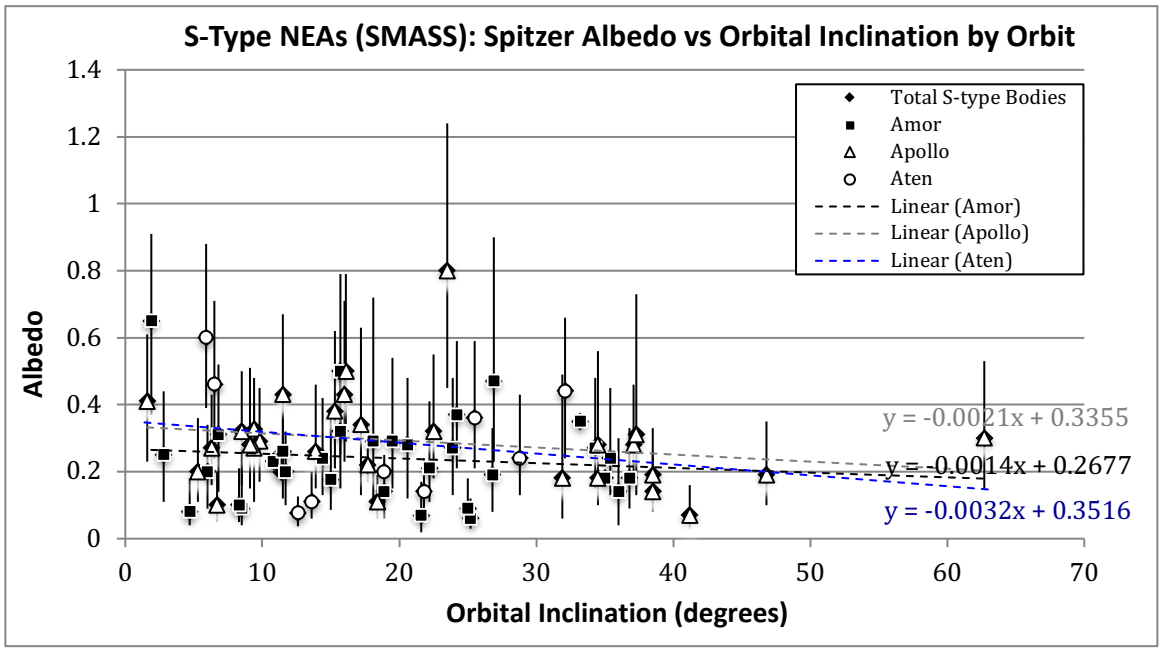

Figure 22. Albedo-inclination regression lines for all S-complex asteroids by orbit type

Plot of albedo-inclination regression lines for the population of S-type and S-subtype asteroids under study, organized by orbit type (e.g., Amor, Apollo, and Aten). Vertical bars represent albedo error (see Table 1).

For the Amor, Apollo, and Aten asteroids in this analysis, it was determined that the absolute values of the calculated correlation coefficient *r*-values of -0.1127, -0.2232, and

-0.1690, respectively, did not exceed the critical values of 0.2094, 0.2207, and 0.4284 at the 75% confidence interval. As a result, these albedo-inclination relationships cannot be shown to be statistically significant. However, despite failing the significance test, it is worth noting that across several asteroid subtypes, the slopes of each of the regression lines by orbit type match the predictions for shallowest-to-steepest for Amor (-0.14% albedo per degree inclination), Apollo (-0.21% albedo per degree inclination), and Aten (-0.32% albedo per degree inclination), respectively.

9.0 CONCLUSIONS AND DIRECTIONS FOR FURTHER RESEARCH

9.1 CONCLUSIONS

Primarily, a statistically-significant relationship was observed between asteroid orbital inclination and albedo for the total population group under study, as well as for one of the spectral classification subgroups. Secondarily, while the remaining subgroups did not show a statistically-significant inclination-albedo relationship, possibly owing to extremely small sample sizes, a significant covariance correlation was observed between the inclination-albedo regression lines generated for each of the subgroups.

Together, these findings validate that the direction of potential correlation between inclination and albedo for each of the subgroups is the same, and further, that the slopes of each of the regression lines agree in a significant way, i.e., they are significantly parallel.

9.2 LIMITATIONS

For the subgroups under study, these findings may at worst indicate unacknowledged bias in the observational methodology relative inclination and albedo. At best, they may indicate that the observed effect is real for each of the S-subtypes but that the sample size is currently insufficient to demonstrate such an effect in a statistically-significant way. It is also worth mentioning that the work of Trilling et al. (2010) shows that observational surveys may necessarily bias datasets against identifying smaller, lower-albedo objects; this may not ultimately alter the slope of any apparent inclination-albedo relationship, but it would act to shift the regression intercept for a dataset toward higher albedos altogether, increasing the noise-to-signal ratio. While no statistically-significant relationship was demonstrated between albedo-inclination and orbit type

in the majority of the subgroups, it is worth pointing out that the overall observed orbit-based trending agreed with what would be expected if "freshening" processes acted on the NEAs with the greatest probability of gravitational interactions, which appears at least on an anecdotal level to reinforce the possibility of an inclination-albedo correlation.

9.3 DISCUSSION AND RECOMMENDATIONS FOR FURTHER RESEARCH

Insight gained by this study includes a possible synthesis of weathering and freshening mechanisms that operate in opposition or in concert with one-another to produce observed weathering patterns. For example, in addition to the potential inclination/ion-bombardment/albedo relationship suggested by some of the study findings, the literature review of space weathering style observed on Mercury suggests a limit with respect to semi-major axis beyond which micrometeorite effects overwhelm ion bombardment effects. This provides two degrees of freedom. Likewise, airless body orbits that venture farther into the inner Solar System and thereby cross a greater number of planetary orbits could be expected to increase the probability of planetary interactions; therefore, they would be expected to produce increased surficial freshening rates acting in opposition to weathering mechanisms. Additionally, it is manifest that an overall increase in airless body mass will enhance micrometeoroid effects due to gravitational acceleration while not appreciably affecting ion bombardment energies, which could provide another rationale for the size-albedo trending explored by Thomas et al. (2014) beyond their general assertion that larger bodies tend to be older and therefore more weathered. Figure 23 presents a schematic attempt to integrate each of these processes into an overall weathering scheme.

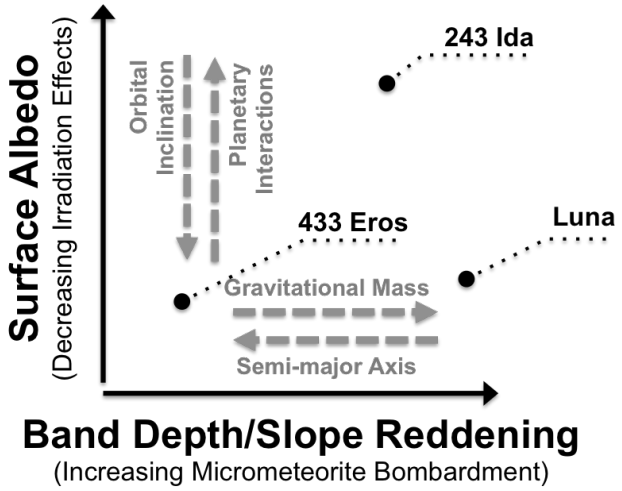

Figure 23. Revised space weathering spectral-orbital-albedo correlation schematic

Combined schematic representation of proposed spectral–albedo and orbital-albedo optical surface correlations, illustrating the hypothetical parameter-space locations of key airless bodies, including the Moon (Luna) and S-type asteroids 243 Ida and 433 Eros. Axis arrows indicate the direction of increasing value, and plotted arrows indicate the apparent direction of effect of each weathering mechanism (Patterned after Gaffey, 2010).

Figure 24, below, attempts an integrated, semi-geographical diagram of these weathering trends as they might operate across the Solar System.

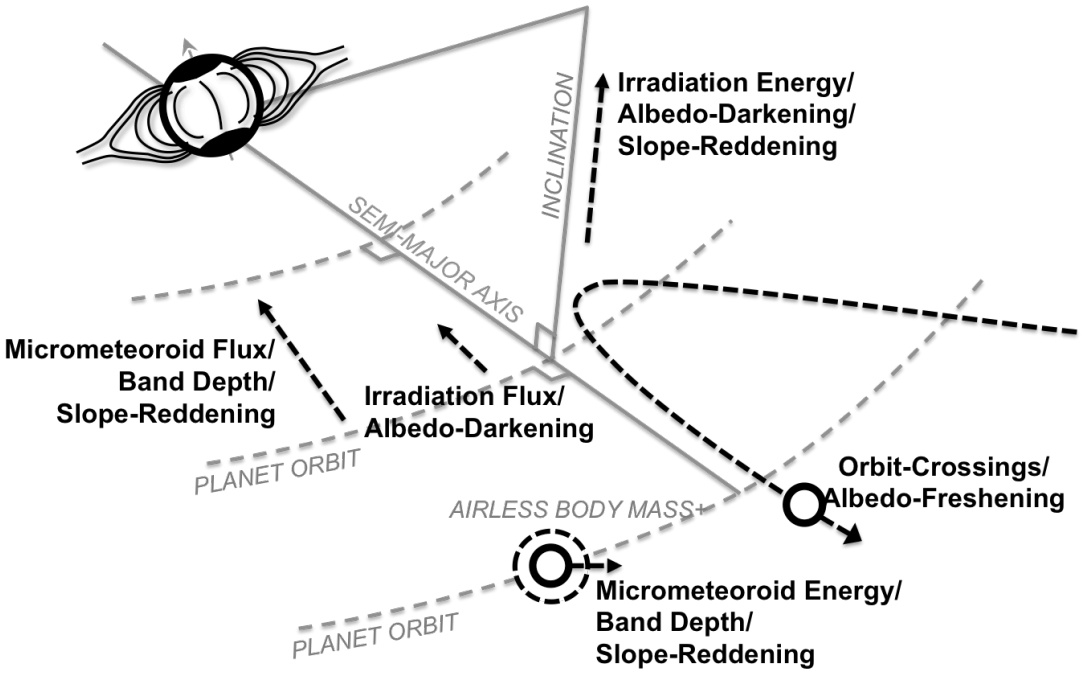

Figure 24. Diagram of proposed spectral-orbital-albedo optical surface correlations

A diagrammatic representation combining the proposed spectral–albedo and orbital-albedo optical surface correlations considered in this study. Arrows indicate the direction of increasing value.

Given the promising correlations observed in portions of the present analysis using an admittedly-restricted dataset, directions for further research include: 1) the collection of new, higher-resolution spectral composition data for additional NEAs in order to increase the study population size, 2) approach the possibility of utilizing alternative S-type datasets to increase the study size, and/or 3) perform a broader inclination-albedo analysis of not only S-type bodies, but other compositional asteroid types, as well. Additionally, given the sustained possibility that high(er)-energy ion bombardment may "prepare" an airless body surface for spectral darkening and the weakening of absorption bands via micrometeorite impacts, the findings of Sasaki et al. (2002) bear particular relevance. Specifically, they found that physical, laser-pulse simulations of micrometeorite impacts on olivine/pyroxene/anorthite pellets acted to produce "significant" reddening and "widespread" accumulation of nanophase iron, while the same simulations on

pure olivine crystals produced no trace of these effects. Likewise, increased significance could be assigned to the suggestion of Brunetto et al. (2007) that the role of iron-containing amorphous or glassy silicates in the overall weathering tendency of target material is deserving of further experimental investigation, which it appears has not been performed to date. Consequently, it is the author's opinion that it would be fruitful to replicate the Sasaki et al. experiment but add precursor ion beam irradiation to simulate fast-solar-wind production of amorphous grains via mictization prior to or coincident with micrometeoroid bombardment. Thereby, the potential for higher-energy ion bombardment to increase a material surface's sensitivity to micrometeorite-impact-driven space weathering effects may be directly explored.

10.0 WORKS CITED

Adams, J. B., & McCord, T. B. (1971). Optical Properties of mineral separates, glass and anorthositic fragments from Apollo mare samples. *Procedings Lunar Science Conference,* 2: 2183-2195.

Bailey, E., Batygin, K., & Brown, M. E. (2016). Solar obliquity induced by planet nine. *The Astronomical Journal,* 152: 5.

Balogh, A., Marsden, R. G., and Smith, E. J., (2001). *The Heliosphere Near Solar Minimum: the Ulysses Perspective.* Chichester, UK: Springer-Praxis.

Balogh, A., Lanzerotti, L. J., and Suess, S. T. (2007). *The Heliosphere through the Solar Activity Cycle.* Chichester, UK: Springer-Praxis.

Bate, R. R., Mueller, D. D., & White, J. E. (1971). *Fundamentals of Astrodynamics.* New York: Dover Publications, Inc.

Bell, J. F., (1988). A probable asteroidal parent body for the CV or CO chondrites. *Meteoritics,* 23: 256-257.

Bell, J. F. et al., (1989). Asteroids: The big picture. In: Binzel, R.P., Gehrels, T., Matthews, M.S. (Eds.), *Asteroids II*. Univ. of Arizona Press, Tuscon, pp. 921-948.

Binzel, R. P., Rivkin, A. S., Stuart, J. S., Harris, A. W., Bus, S. J., and Burbine, T. H. (2004). "Observed Spectral Properties of Near-Earth Objects: Results for Population Distribution, Source Regions, and Space Weathering Processes." *Icarus,* 170: 259-294.

Binzel et al., (2010). Earth encounters as the origin of fresh surfaces on near-Earth asteroids. *Nature Letters,* 463: 331-334.

Blewett, D. T., Denevi, B. W., Le Corre, L., Reddy, V., Schroder, S. E., Pieters, C. M., et al. (2016). Optical space weathering on Vesta: Radiative-transfer models and Dawn observations. *Icarus,* 265: 161-174.

Blewett, D. T., Denevi, B. W., Robinson, M. S., Ernst, C. M., Purucker, M. E., & Solomon, S. C. (2010). The apparent lack of lunar-like swirls on Mercury: Implications for the formation of lunar swirls and for the agent of space weathering. *Icarus,* 209: 239-246.

Brunetto, R., & Strazzulla, G. (2005). Elastic collisions in ion irradiation experiments: A mechanism for space weathering of silicates. *Icarus*, 179: 265-27.

Brunetto, R., Roush, T. L., Marra, A. C., & Orofino, V. (2007). Optical characterization of laser ablated silicates. *Icarus*, 191: 381-393.

Bus, S. J., & Binzel, R. P. (2002). Phase II of the Small Main-belt Asteroid Spectroscopy Survey: A feature-based taxonomy. *Icarus,* 158: 146-177.

Cloutis, E. A., Gaffey, M. J., Jackowski, T. L., & Reed, K. L., (1986). Calibrations of phase abundance, composition, and particle size distribution of olivine–orthopyroxene mixtures from reflectance spectra. *Journal of Geophysical Research,* 91: 11641-11653.

DeMeo, F. E., Binzel, R. P., & Lockhart, M. (2014). Mars encounters cause fresh surfaces on some near-Earth asteroids. *Icarus*, 227: 112-122.

Djurabekova, F., Samela, J., Timko, H., Nordlund, K., Calatroni, S., Taborelli, M., & Wuensch, W. (2012). Crater formation by single ions, cluster ions and ion "showers." *Nuclear Instruments and Methods in Physics Research B,* 272: 374-376.

Dunn, T. L., Burbine, T. H., Bottke Jr., W. F., & Clark, J. P. (2013). Mineralogies and source regions of near-Earth asteroids. *Icarus,* 222: 273-282.

Durante, M., & Cucinotta, F. A. (2011). Physical basis of radiation protection space travel. *Review of Modern Physics*, 1245-1250.

El-Baz, F. (1972). The Alhazen to Abul Wafa swirl belt: An extensive field of light-colored sinuous markings. *NASA Special Publication* 315: 29-93.

Farrel, W. M., Hurley, D. M., & Zimmerman, M. I. (2015). Solar wind implantation into lunar regolith: Hydrogen retention in a surface with defects. *Icarus,* 255: 116-126.

Gaffey, M. J., Burbine, T. H., & Binzel, R. P. (1993). Asteroid spectroscopy: progress and perspectives. *Meteoritics,* 28: 161-187.

Gaffey, M. J. (2010). Space weathering and the interpretation of asteroid reflectance spectra. *Icarus,* 209: 564-567.

Gosling, J. T., & Pizzo, V. J., (1999). Formation and evolution of corotating interaction regions and their three dimensional structure. *Space Scence Reviews,* 89: 21-52.

Grun, E., et al. (1992a). The Ulysses dust experiment. *The Astrophysical Journal Supplement Series*, 92: 411-423.

Grun, E., et al. (1992b). The Galileo dust detector. *Space Science Reviews*, 60: 317-340.

Grun, E., et al. (1997). South-North and Radial Traverses through the Interplanetary Dust Cloud. *Icarus*, 129: 270-288.

Hapke, B. (2001). Space weathering from Mercury to the asteroid belt. *Journal of Geophysical Research,* 106: 10039-10073.

Hapke, B., Cassidy, W., & Wells, E. (1975). Effects of vapor-phase deposition process on the optical, chemical and magnetic properties of the lunar regolith. *Moon,* 13: 339-353.

Harris, A. W., et al. (2011). ExploreNEOs. II. The accuracy of the Warm Spitzer near-Earth object survey. *The Astronomical Journal*, 141: 75.

Heller, C. H. (1993). Encounters with protostellar discks. 1. Disk tilt and the nonzero solar obliquity. *The Astrophysical Journal,* 408: 337-346.

Hemingway, D. J., Garrick-Bethell, I., & Kreslavsky, M. A. (2015). Latitudinal variation in spectral properties of the lunar maria and implications for space weathering. *Icarus,* 261: 66-79.

Hendrix, A., & Vilas, F. (2006). The effects of space weathering at UV wavelengths: S-class asteroids. *The Astronomical Journal,* 132 (3): 1396-1404.

Killen, R.M. et al. (2012). The effect on the lunar exosphere of a coronal mass ejection passage. *Journal of Geophysical Research, 117*, E00K02.

Kissel, J., and Kruger, F. R. (1987). Ion formation by impact of fast dust particles and comparison with related techniques. *Applied Physics A*, 42: 69-85.

Kohout, T., Cuda, J., Filip, J., Britt, D., Bradley, T., Tucek, J., et al. (2014). Space weathering simulations through controlled growth of iron nanoparticles on olivine. *Icarus,* 237: 75-83.

Kruger, H., et al. (2010). Three years of Ulysses dust data: 2005 to 2007. *Planetary and Space Science*, 58: 951-964.

Majaess, D. J., Tanner, J., Savoy, J., & Sampson, B. (2008). 349 Dembowska: A Minor Study of its Shape and Parameters. *Minor Planet Bulletin,* 35: 88.

Mueller, M., et al. (2011). ExploreNEOs. III. Physical characterization of 65 potential spacecraft target asteroids. The *Astronomical Journal*, 141:109.

Natrella, M. G., (2005). *Experimental Statistics.* Mineola, New York: Dover Publications.

NEOSurvey, 8 Aug. 2016, "NEOSurvey--results," online at *Near-Earth Objects at Northern Arizona University* [http://neareathobjects.nau.edu/neosurvey/results.html

Ness, R. G., and J. P. Emery, 2014, Thermal inertia estimates of four near-Earth asteroids from Spitzer Space Telescope spectral observations, *Abstracts of Papers Submitted to the Lunar and Planetary Science Conference*, 45: 1430.

Noble, S. K., Hiroi, T., Keller, L. P., Rahman, Z., Sasaki, S., & Pieters, C. M. (2011). Experimental space weathering of ordinary chondrites by nanopulse laser: TEM results. *Abstracts of Papers Submitted to the Lunar and Planetary Science Conference,* 42: 1382.

Noble, S. K., Pieters, C. M., & Keller, L. P. (2007). An experimental approach to understanding the optical effects of space weathering. *Icarus,* 192: 629-642.

Noble, S. K., Pieters, C. M., Taylor, L. A., Morris, R. V., Allen, C. C., McKay, D. S. (2001). The optical properties of the finest fraction of lunar soil: Implications for space weathering. *Meteoritics and Planetary Science,* 36: 31-42.

Noguchi, T., et al. (2011). Incipient space weathering observed on the surface of Itokawa dust particles. *Science*, 333: 1121-1124.

Pieters, C. M., Taylor, L. A., Noble, S. K., Keller, L. P., Watson, B., Morris, R. V., Allen, C. C., McKay, D. S., & Wentworth, S. (2000). Space weathering on airless bodies: Resolving a mystery with lunar samples. *Meteoritics and Planetary Science,* 35: 1101-1107.

Pizzo, V. J. (1991). The evolution of corotating stream fronts near the ecliptic plane in the inner solar system 2. Three-dimensional tilted dipole fronts. *Journal of Geophysical Research,* 96: 5405.

Poppe, A. R., Fatemi, S., Garrick-Bethell, I., Hemingway, D., & Holmstrom, M. (2016). Solar wind interaction with the Reiner Gamma crustal magnetic anomaly: Connecting source magnetization to surface weathering. *Icarus*, 266: 261-266.

Rodriguez-Nieva, J. F., & Bringa, E. M. (2013). Molecular dynamics and Monte Carlo simulations of the sputtering of a nanoporus solid. *Nuclear Instruments and Methods in Physics Research B,* 304: 23-26.

Rodriguez-Nieva, J. F., Bringa, E. M., Cassidy, T. A., Johnson, R. E., Caro, A., Fama, M., et al. (2011). Sputtering from a porus material by penetrating ions. *The Astrophysical Journal Letters,* 743: L5.

Sarantos, M., Killen, R. M., & Kim, D. (2007). Predicting the long-term solar wind ion-sputtering source at Mercury. *Planetary and Space Science,* 55: 1584-1585.

Sasaki, S., & Kurahashi, E. (2004). Space weathering on Mercury. *Advances in Space Research,* 33: 2152-2155.

Sasaki, S., Nakamura, K., Hamabe, Y., Kurahashi, E., & Hiroi, T. (2001). Production of iron nanoparticles by laser irradiation in a simulation of lunar-like space weathering. *Nature*, 555-557.

Starkuhina, L. V. (2006). Polar regions of the Moon as a potential repository of solar-wind implanted gases. *Advances in Space Research,* 37: 50-58.

Suess, S. (1999, June 3). *Ulysses Results "Bimodality"*. Retrieved December 5, 2015, from Marshall Space Flight Center Solar Physics: http://solarscience.msfc.nasa.gov/people/suess/SolarProbe/Page3.htm

Tholen, D. J. (1989). Asteroid taxonomic classifications. *Asteroids II.* (pp. 1139-1150) Tuscon: University of Arizona Press.

Thomas, C. A., et al. (2011). ExploreNEOs. V. Average albedo by taxonomic complex in the near-Earth asteroid population. *The Astronomical Journal*, 142: 85.

Thomas, C. A., et al. (2014). Physical characterization of Warm Spitzer-observed near-Earth objects. *Icarus*, 228: 217.

Tribble, A. C. (2003). *The Space Environment.* Princeton, NJ: Princeton University Press.

Trilling, D. E. et al., (2010). EXPLORENEOs. I. Description and first results from the Warm Spitzer near-Earth object survey. *The Astronomical Journal*, 140: 770-784

Zinkle, S. J. (2012). Radiation-Induced Effects on Microstructure. In R. J. Konings, *Comprehensive Nuclear Materials* (pp. 65-98). Amsterdam: Elsevier.